Delft University of Technology

Document Version
Final published version

Licence
CC BY

Citation (APA)
Babu, R. S., Madai, E., Nair, D. S., Gonugunta, P., Armaki, S. M., Hendrikx, R., Panneerselvam, T., Murugan, R., Kumar, V. V. R. K., Taheri, P., Mol, A., Satyanarayana, N., & Anusuyadevi, P. R. (2025). Effect of synthesis conditions on morphology, surface chemistry and electrochemical performance of nickel ferrite nanoparticles for lithium-ion battery applications. *Journal of Materials Science: Materials in Electronics*, *36*(14), Article 865. https://doi.org/10.1007/s10854-025-14886-w

Important note
To cite this publication, please use the final published version (if applicable).
Please check the document version above.

Copyright
In case the licence states “Dutch Copyright Act (Article 25fa)”, this publication was made available Green Open Access via the TU Delft Institutional Repository pursuant to Dutch Copyright Act (Article 25fa, the Taverne amendment). This provision does not affect copyright ownership.
Unless copyright is transferred by contract or statute, it remains with the copyright holder.

Sharing and reuse
Other than for strictly personal use, it is not permitted to download, forward or distribute the text or part of it, without the consent of the author(s) and/or copyright holder(s), unless the work is under an open content license such as Creative Commons.

Takedown policy
Please contact us and provide details if you believe this document breaches copyrights.
We will remove access to the work immediately and investigate your claim.

This work is downloaded from Delft University of Technology.

J Mater Sci: Mater Electron **(2025) 36:865**

Effect of synthesis conditions on morphology, surface chemistry and electrochemical performance of nickel ferrite nanoparticles for lithium-ion battery applications

Reshma S Babu[1], Eszter Madai[2], Durga S Nair[3], Prasad Gonugunta[2], Seyedamirhossein Mohseni Armaki[2], Ruud Hendrikx[2], Thamayanthi Panneerselvam[1], Ramaswamy Murugan[1], V. V. Ravi Kanth Kumar[1], Peyman Taheri[2], Arjan Mol[2], N. Satyanarayana[1,*], and Prasaanth Ravi Anusuyadevi[2,*]

[1] *Department of Physics, Pondicherry University, Puducherry 605014, India*
[2] *Department of Materials Science and Engineering (MSE), Faculty of Mechanical Engineering (ME), Delft University of Technology, Mekelweg 2, 2628 CD Delft, The Netherlands*
[3] *Department of Physics, Puducherry Technological University, Puducherry 605014, India*

Received: 12 November 2024
Accepted: 28 April 2025
Published online: 23 May 2025

© The Author(s), 2025

ABSTRACT

In the search for effective high-tech materials for energy conversion and storage devices, spinel-structured nickel ferrite ($NiFe_2O_4$) has been identified as a promising anode material for lithium-ion batteries (LIBs). However, the influence of different morphologies and surface properties of $NiFe_2O_4$ nanoparticles on battery performance is hardly addressed. To understand the effect of different morphologies and surface properties on the lithium-ion storage performance, $NiFe_2O_4$ nanoparticles were synthesized through four different synthesis conditions: NFO-S, NFO-U, NFO-G, and NFO-C. The formation of polycrystalline inverse spinel $NiFe_2O_4$ was confirmed through XRD, FTIR, and Raman spectroscopy. The morphologies of the obtained samples were studied using FESEM, and it was found that the four different synthesis conditions employed here enabled us to obtain $NiFe_2O_4$ with four different morphologies. The surface chemistry, surface area and porosity of the $NiFe_2O_4$ samples were respectively characterized using XPS and BET. The electrochemical performance of the four $NiFe_2O_4$ samples as anode material was studied by fabricating lithium-ion half-cells. $NiFe_2O_4$ sample obtained from surfactant-free synthesis condition (NFO-S) displayed a high initial discharge and charge capacity of 2258 mAh/g and 1815 mAh/g, respectively at the current density of 100 mA/g. Even after 100 cycles, NFO-S showed a better discharge capacity of 116 mAh/g at the current density of 100 mA/g, compared to the other samples studied here. The observed higher capacity of the NFO-S sample is attributed to the higher surface area (40.8 m^2/g) and pore volume (0.190 cm^3/g).

Address correspondence to E-mail: nallanis2011@gmail.com; P.RaviAnusuyadevi@tudelft.nl; ranu.prasaanth@gmail.com

https://doi.org/10.1007/s10854-025-14886-w

The $NiFe_2O_4$ sample prepared with cationic CTAB surfactant (NFO-C) showed better cyclic stability with a stable coulombic efficiency of 98.5% at the 100th cycle, mainly attributed to its nanocube morphology with lower surface area (16.1 m^2/g) and pore volume (0.087 cm^3/g).

1 Introduction

Environmental issues related to excessive usage of non-renewable energy resources have led to ever-increasing intensive research of alternatives, in particular during the last decades. Persistently, there is a high demand for fast rechargeable and weightless batteries with long cyclic life and high energy density [1, 2]. Currently, high energy density storage devices with long cyclic life are required for various applications: storage of renewable energy, electric vehicles, and fast-developing portable electronic devices like digital cameras, mobile phones, laptops, etc. Lithium-ion batteries (LIBs) are found to be the most suitable choice due to their long cyclic life, good energy density, wide operating temperature range, and low memory effect [3–6].

Graphite is widely used as the anode material in commercial LIBs, since it is economical and has a good cyclic life. However, the low specific capacity of graphite (372 mAh/g) is a significant limitation [3, 7]. As an alternative material for the anode in LIBs, transition metal oxides (TMOs) were introduced [7, 8]. Mainly three types of lithium-ion storage mechanisms occur in the anode of LIBs: intercalation, alloying, and conversion reaction. TMOs undergo a conversion reaction with lithium and this effectively utilizes all possible oxidation states of TMOs [8–13]. During discharging, the transition metal oxide anode gets reduced to the transition metal, and during charging, metals get re-oxidized to metal oxide, which helps achieve a longer cyclic life. Therefore, most of the TMOs have a better theoretical capacity than graphite. TMOs have crystal structures such as spinel, perovskite, rutile, etc., which enhance lithium storage capacity [14, 15]. Despite the advantages, TMOs exhibit low electrical conductivity and significant volume variation during the charge–discharge cycles [16–18].

Among spinel oxides with the formula AB_2O_4, ferrites stand out with their lithium cyclability, theoretical capacity, non-toxicity, and abundance. Its spinel structure can accommodate eight lithium ions [12, 19, 20]. Spinel oxides, such as $LiMn_2O_4$ are also used as cathode materials in LIBs due to their enhanced energy densities [21]. The mixed metal oxides can have a normal spinel, inverse spinel or mixed spinel structure depending on the metal ion radius and its oxidation state [17, 22, 23]. Also, the synergistic effect from two metals in binary transition metal oxide shows enhanced performance. $NiFe_2O_4$ (NFO) has a high theoretical capacity of 915 mAh/g and an inverse spinel structure, as shown in Fig. 1, where octahedral sites are filled with Ni^{2+} ions and half of Fe^{3+} ions and tetrahedral sites with another half of Fe^{3+} ions [24–27]. Hence, one mole of $NiFe_2O_4$ reacts with 8 mol of lithium providing a high theoretical capacity [4, 28, 29]. $NiFe_2O_4$ is a non-toxic compound, while nickel and iron are abundant on the earth [30]. However, $NiFe_2O_4$ has some demerits such as low electrical conductivity, large volume expansion and hysteresis in voltage during charge–discharge, which should be taken into account. Mesoporous nanostructured $NiFe_2O_4$ can improve the electrochemical performance by providing more active sites for the reaction and can also accommodate the volume changes during continuous cycling [4, 31, 32]. The conductivity and the electrochemical performance can be increased by adding carbonaceous materials like carbon nanotubes, nanosphere, quantum dots or graphene oxides. The conductive carbon materials with high surface area and porosity increase the cyclic life, by mitigating the volume expansion during cycling [33–47].

The present study stands out from the previous studies, majorly focusing on the effect of different morphology, surface properties, porosity and surface chemistry on the lithium storage performance of $NiFe_2O_4$ nanoparticle samples prepared under four different synthesis conditions. This will provide fundamental knowledge towards optimizing $NiFe_2O_4$-based composite morphologies, solving their intrinsic

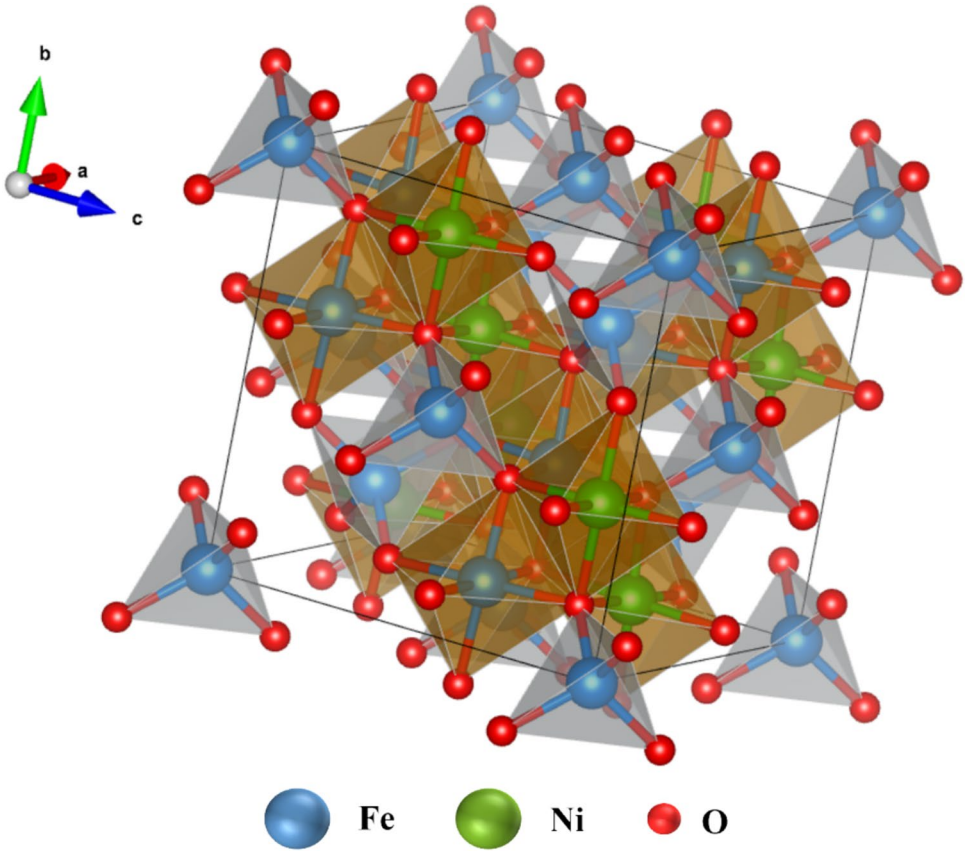


Fig. 1 Inverse spinel structure of Nickel ferrite ($NiFe_2O_4$) unit cell with 32 O^{2-} ions, 8 Ni^{2+} ions, and 16 Fe^{3+} ions

conductivity issues and achieving efficient LIBs with $NiFe_2O_4$ as an anode material for the future. To attain a better understanding of how $NiFe_2O_4$ morphological changes affect the lithium storage performance, and to extract the best out of them, hydrothermally synthesized $NiFe_2O_4$ nanomaterials were studied as an anode in LIBs. In this work, we developed different morphologies of $NiFe_2O_4$ nanoparticles through the four different synthesis conditions, as shown in Figs. 2 and S1 from Supporting Information. By varying the additives, reaction temperature, and reaction time, different morphologies of $NiFe_2O_4$ nanoparticles were developed. Thus, the obtained $NiFe_2O_4$ materials exhibited different morphology, surface area, porosity, and surface chemistry, which displayed a significant influence on the performance of LIBs. Therefore, this study aims to investigate how different particle size, morphology, surface area, porosity, and surface chemistry of $NiFe_2O_4$ nanoparticles developed through different conditions of hydrothermal synthesis influence their electrochemical properties. The synthesis conditions employed here are optimized to find the best-performing $NiFe_2O_4$ as anode in LIBs. As the four different synthesis conditions are newly designed in this work, it produced nickel ferrite nanoparticles with different morphologies which were not reported before with similar precursors, precipitants and/or surfactants in the domain of hydrothermal synthesis. The newly reported batch-reactor parameters of this study can be implemented in the future using continuous supercritical synthesis techniques, where such advanced protocols pave the way for large-scale production of nanomaterials for energy storage applications [48, 49].

The phase purity and crystalline structure of the four as-synthesized $NiFe_2O_4$ nanoparticle samples were studied by XRD. Lattice structure and metal ion distribution within the inverse spinel cubic sublattice were studied using ATR-FTIR and Raman spectroscopy. The effect of (co)-precipitants and surfactants on the particle size and morphology of $NiFe_2O_4$ nanoparticle samples was studied by FESEM, and the

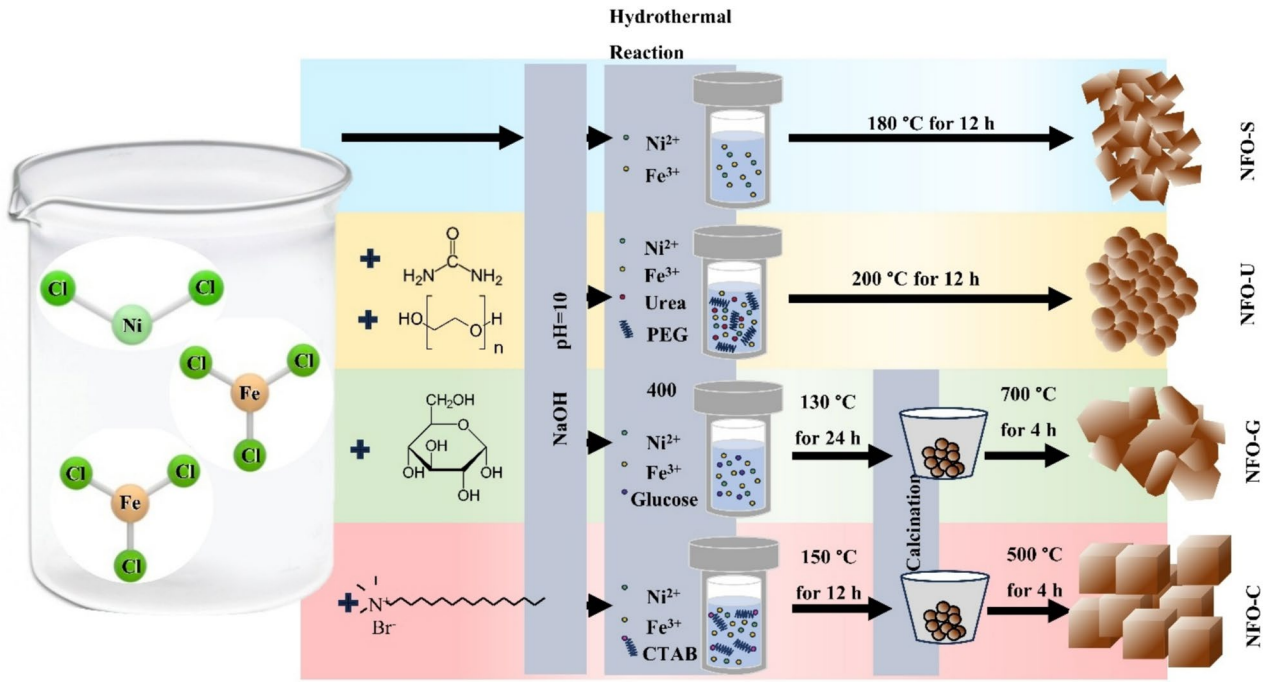


Fig. 2 Schematic representation of four different synthesis conditions for producing $NiFe_2O_4$ nanoparticle samples (NFO-S, NFO-U, NFO-G, NFO-C)

corresponding elemental mapping was achieved by EDX analysis. The surface chemistry with the distribution of metal ions and their corresponding valance states were studied using XPS. The surface properties and porosity were studied by the N_2 adsorption–desorption technique.

The lithium storage performance of the samples was studied by fabricating a half-cell consisting of $NiFe_2O_4$ as the working electrode and lithium as the counter electrode. Cyclic voltammetry (CV), galvanostatic charge–discharge (GCD), and electrochemical impedance spectroscopy (EIS) techniques were used to study the electrochemical performance of the samples. CV was performed to understand the redox reactions occurring during the charge–discharge cycles of the lithium-ion cells. CV demonstrated the capacity fading and cyclic stability of NFOs. GCD was employed to assess the electrochemical performance of the developed nickel ferrite nanoparticles over continuous charge–discharge cycles, whereas EIS was performed to understand the resistive and capacitive response offered by the components of the electrochemical system.

2 Materials and methods

2.1 Synthesis of nanoparticles

Nickel ferrite ($NiFe_2O_4$) nanoparticles were synthesized by a hydrothermal route using different co-precipitants and/or surfactants, under different temperatures and reaction times. Nickel chloride hexahydrate ($NiCl_2{\cdot}6H_2O$, 98%, Sigma-Aldrich) and anhydrous ferric chloride ($FeCl_3$, 98%, Sigma-Aldrich) were used in 1:2 molar ratio, to prepare the precursor solution. This solution was brought to pH 10, by dropwise addition of 1 M sodium hydroxide (NaOH, 97%, SRL) solution. The resultant 100 mL solution was poured into a 200 mL Teflon-lined autoclave and kept for hydrothermal reaction. The obtained product was centrifuged and washed several times with deionized water. The washed residue was dried at 80 °C in a hot-air oven overnight.

- The $NiFe_2O_4$ nanoparticle sample synthesized at 180 °C for 12 h was named as NFO-S.
- The $NiFe_2O_4$ nanoparticles synthesized in the presence of urea (99%, SRL) and polyethylene glycol 400 (PEG400, Sigma-Aldrich) at 200 °C for 12 h was named as NFO-U.

- The $NiFe_2O_4$ nanoparticles synthesized in the presence of D-glucose (SRL) at 130 °C for 24 h and calcinated at 700 °C for 4 h was named as NFO-G.
- The $NiFe_2O_4$ nanoparticles synthesized in the presence of cetyltrimethylammonium bromide (CTAB, 99%, SRL) at 150 °C for 12 h and calcinated at 500 °C for 4 h was named as NFO-C.

All $NiFe_2O_4$ samples prepared under four different synthesis conditions were ground using a mortar and a pestle for further studies. Figures 2 and S1 in Supporting Information respectively show the schematic diagram and flowchart of the complete synthesis process of $NiFe_2O_4$ nanoparticles produced by the four different synthesis conditions.

2.2 Characterization

For all the prepared $NiFe_2O_4$ samples, X-ray Diffraction (XRD) patterns were recorded using the Bruker D8 Advance diffractometer (Cu K_α radiation, $\lambda = 1.54$ Å), in the range of 10°–80° with a step size of 0.02° 2Θ. The powder samples were deposited on a Si510 zero-background wafer during measurements, and their corresponding XRD data were evaluated using Bruker-AXS software DiffracSuite.EVA 7.2 and Panalytical Highscore. Fourier transform infrared (FTIR) spectra were obtained using a Thermo Nicolet iS50-FTIR in Attenuated Total Reflectance (ATR) mode with 4 cm^{-1} resolution. Raman spectra have been obtained using a WiTeC Alpha300R Raman imaging microscope, using a 532 nm laser with 0.5 mW laser power to avoid damaging the samples with an integration time of 8 s and 10 accumulations. The samples for Raman measurements were prepared by dissolving sample powder in isopropyl alcohol (IPA) and drop cast on quartz slides. The morphologies of the as-synthesized $NiFe_2O_4$ nanoparticles were characterized using field emission scanning electron microscopy (FESEM, JEOL, JSM-6500F) at an accelerating voltage of 20 kV and a working distance of 10 mm. The FESEM images during Energy-Dispersive X-ray spectroscopy (EDX) were captured at a 25 mm working distance and 20 kV accelerating voltage. The surface chemistry of $NiFe_2O_4$ nanoparticles was studied using a PHI 5400 XPS (X-ray Photoelectron Spectroscopy) (Physical Electronic Inc.), possessed with an Aluminum (Al)-non-monochromatic K_α X-ray radiation ($h\nu = 1486.7$ eV). This X-ray was provided with a 200 W power setting at 13.5 kV accelerating electron voltage. XPS measurements were carried out at 10^{-9} mbar vacuum, the pass energy during the full survey measurement was 89.45 eV, and the pass energy at high-resolution measurements was 71.55 eV. All the XPS spectra were processed using MultiPak v.8.0, provided by Physical Electronics Inc., enabling us with facile and precise curve fitting. The Brunauer–Emmett–Teller (BET) surface area and Barrett–Joyner–Halenda (BJH) pore volume were calculated by the N_2 adsorption method using the Micromeritics BET analyzer. The samples were degassed at 120 °C overnight and were analyzed under the N_2 adsorption–desorption technique.

2.3 Electrochemical measurements

For the electrode preparation, the $NiFe_2O_4$ as an active material, polyvinylidene fluoride (PVDF) as binder, and conductive carbon are taken in an 8:1:1 ratio and mixed with N-methyl pyrrolidone (NMP). The well-mixed slurry is coated on the copper foil using a doctor blade and dried at 120 °C overnight. The dried electrode was cut in 8 mm diameter size using an electrode disk cutter. CR2032 coin cell-type lithium-ion batteries were fabricated using the NFO-S/ NFO-U/NFO-G/ NFO-C nanoparticles as the working electrode, lithium metal as the counter electrode, 1 M $LiPF_6$ in EC: EMC (1:1) as the electrolyte, and Whatman glass fiber filter as the separator. All the cells were assembled in the argon filled glove box. The cells were characterized by measuring cyclic voltammetry (CV), charge–discharge measurements, and electrochemical impedance spectroscopy (EIS) using the electrochemical workstation of Biologic BCS-810. CV has been performed by varying the voltage range 0.01–3 V at a scan rate of 0.1 mV/s and measuring the respective current for five cycles. At 100 mA/g current density, the charge–discharge studies are performed between 0.01 and 3 V for 100 cycles. EIS measurements were done in the 10 kHz–1 Hz frequency range.

3 Results and discussion

Figure 3a shows the XRD patterns of $NiFe_2O_4$ samples prepared under four different synthesis conditions of NFO-S, NFO-U, NFO-G, and NFO-C. For all the four samples, the observed diffraction peaks are at 2Θ angles of 18.4°, 30.3°, 35.6°, 37.3°, 43.3°, 53.8°, 57.3°, 62.9°, and 74.5°, which were compared with the standard pattern of $NiFe_2O_4$ (ICDD data: 98-011-6755)

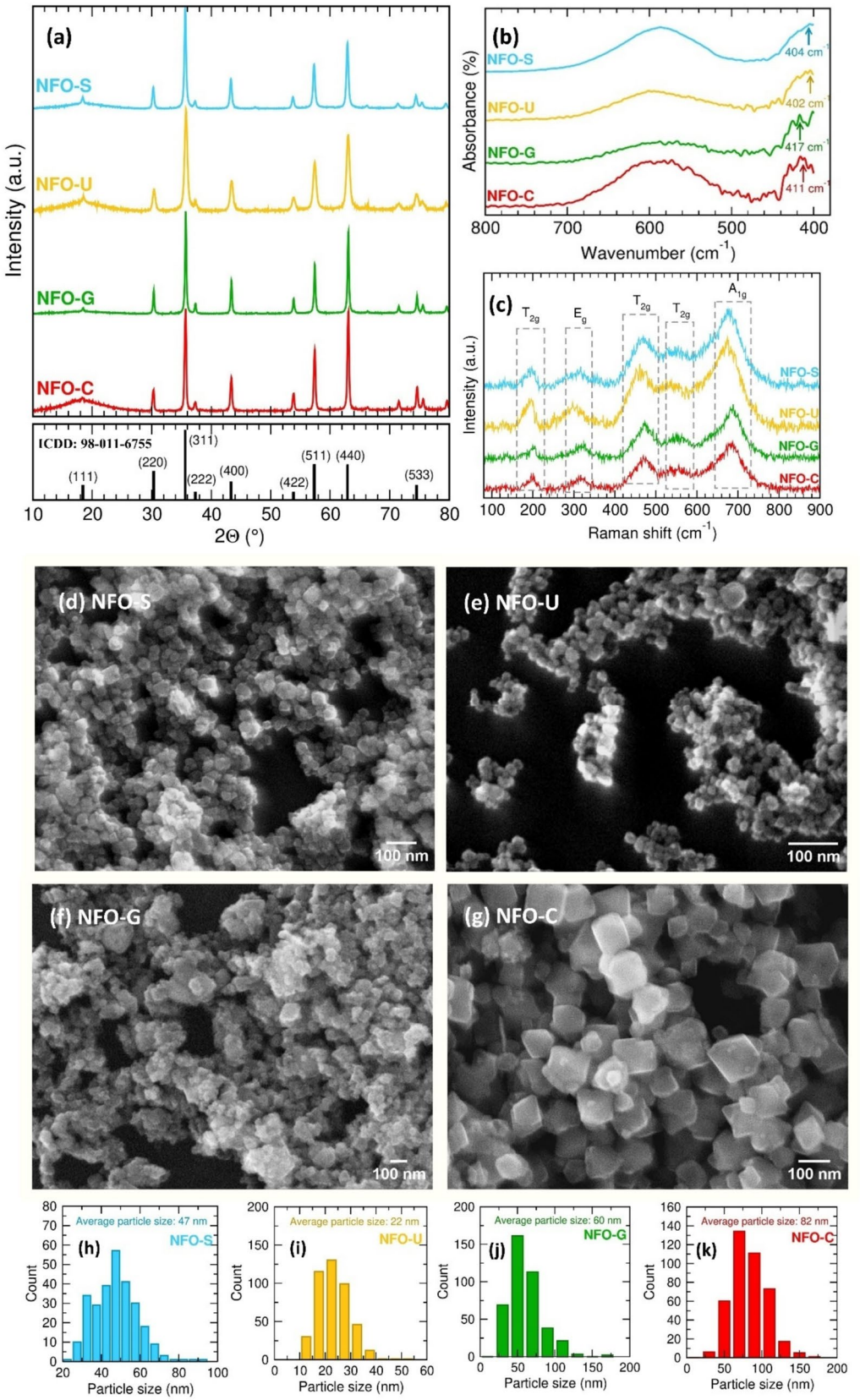


Fig. 3 **a** XRD pattern, **b** FTIR spectra, **c** Raman spectra, **d**–**g** FESEM images and **h**–**k** particle size distribution histograms of NFO-S, NFO-U, NFO-G and NFO-C

and were respectively assigned to (111), (220), (311), (222), (400), (422), (511), (440), and (533) planes [50]. Hence, the formation of the pure crystalline phase of the face-centered cubic (FCC) inverse spinel structure of $NiFe_2O_4$ with space group Fd $\bar{3}$m is confirmed [10, 27, 51, 52]. From Fig. 3a, all four XRD patterns showed an additional broader peak between 12° and 24° with varied intensities, which may be due to the amorphous phase of a minor quantity of impurity. Hence, for all samples including the NFO-C, the XRD peak at 18.4° is overlapped over the additional broader peak between 12° and 24°. This intensity of the broader peak is higher for NFO-C and smaller for NFO-G.

The X-ray diffraction peak broadening is due to the following reasons: (1) Instrumental broadening, (2) Increase in crystallite size, and (3) Lattice strain due to distortion [53]. Thus, the observed total diffraction peak broadening (β_T) can be mathematically related using Eq. (1).

$$\beta_T = \beta_D + \beta_S. \tag{1}$$

Here (β_D) corresponds to the instrumental corrected peak broadening induced due to the crystallite size of $NiFe_2O_4$ nanoparticles only, see Eq. (2) [54]. β_S represents diffraction peak broadening due to the lattice strain and its relation with micro-strain (ε) due to crystal distortion and imperfection is provided by Eq. (3).

$$\beta_D = \frac{k\lambda}{D\cos\theta}, \tag{2}$$

where k is the shape factor, λ is the wavelength of the X-ray, D is the crystallite size (nm), and θ is the Bragg diffraction angle corresponding to the diffraction peak [4, 17, 54].

$$\beta_S = 4\varepsilon\tan\theta. \tag{3}$$

Thus, Eq. (1) can be further simplified, resulting in Eqs. (4) and (5).

$$\beta_T = \frac{k\lambda}{DCos\theta} + 4\varepsilon\tan\theta, \tag{4}$$

$$\frac{\beta_T\cos\theta}{k\lambda} = \frac{1}{D} + \frac{4\varepsilon\sin\theta}{k\lambda}. \tag{5}$$

Thus, through a Williamson–Hall (W–H) analysis plot, using Eq. (5), the crystallite sizes of the $NiFe_2O_4$ particles prepared under four different synthesis conditions were estimated and their crystallite sizes are given in Table 1.

Table 1 Crystallite sizes calculated for four $NiFe_2O_4$ samples studied in this work

$NiFe_2O_4$ samples	Crystallite size (D)
NFO-S	37 ± 3 nm
NFO-U	19 ± 2 nm
NFO-G	51 ± 3 nm
NFO-C	34 ± 3 nm

From Table 1, it is observed that $NiFe_2O_4$ prepared under the NFO-U condition exhibits the smallest crystallite size, whereas the NFO-G sample exhibits the highest crystallite size. The reason for NFO-G and NFO-C samples showing good crystallinity is due to the high-temperature calcination at 500 °C and 700 °C, respectively, whereas the smaller crystallite size of the NFO-U sample may be due to its synthesis involving urea and PEG400 and the absence of the post-calcination step. Further, the XRD results of the directly obtained NFO-G and NFO-C samples, prior to the calcination step, showed impurity phases; hence the NFO-G and NFO-C samples were calcinated to remove the impurity phases, whereas the NFO-S and NFO-U samples obtained directly showed a pure crystalline phase and hence, these samples were not subjected to a post-calcination process.

The inverse spinel structure of $NiFe_2O_4$ allots the distribution of metal ions (especially Fe^{3+}) in the octahedral and tetrahedral sites, localizes the Ni^{2+} ions only in the octahedral site of the sublattice. The two protuberant absorption bands in Fig. 3b of the ATR-FTIR spectra confirm the presence of iron (Fe^{3+}) cations at the different sites of the single-phase crystal structure. The intense band (ν_1) observed in the region of 500–700 cm^{-1} in all the $NiFe_2O_4$ samples in this work, corresponds to the stretching vibrations of the iron-oxygen (Fe^{3+}–O^{2-}) bonding in the tetrahedral site, whereas the second apparent band in the region of 400–430 cm^{-1} corresponds to the metal–oxygen bonds' stretching vibration in the octahedral site [55]. Importantly, ν_2 was centered at 404, 404, 417, and 411 cm^{-1} for NFO-S, NFO-U, NFO-G, and NFO-C, respectively. Such a prominent shift in the absorption position of the FTIR spectrum is due to the difference in the distance between the (Fe^{3+}–O^{2-}) bonds in the octahedral site. Thus, with the introduction and increment of calcination temperature (500–700 °C) in our synthesis protocol, there is a significant enhancement of intensity and shift of the absorption mode to a higher wavenumber,

especially for ν_2 band. This is specifically due to the increase of force constants of the metal–oxygen bonds. However, no such significant order was observed for the broad ν_1 band (500–700 cm^{-1}) for all four $NiFe_2O_4$ samples [56–58].

The observation of active five Raman bands: $A_{1g} + E_g + 3T_{2g}$ in Fig. 3c again substantiates the formation of inverse spinel structure with $Fd\bar{3}m$ space group in all the four $NiFe_2O_4$ nanoparticles. Here, A_{1g} (630–750 cm^{-1}) mode corresponds to the symmetric stretching of the oxygen atoms in the metal–oxygen bonds of the tetrahedral site. The remaining three T_{2g} (150–230, 420–510 and 520–600 cm^{-1}) bands and E_g (280–350 cm^{-1}) correspond to the symmetric bending and asymmetric bending of the metal–oxygen bonds present in the octahedral site, respectively. In the case of NFO-G and NFO-C, due to high-temperature calcination (≥ 500 °C), the Raman bands are narrower and subsequently shift to high frequency due to the redistribution of cations. However, the broadening of Raman bands along with peaks shift to lower frequency, in case of NFO-S and NFO-U, is due to the phonon confinement effect, arising from its smaller nanoparticle size [55, 56, 59, 60].

The morphology of our $NiFe_2O_4$ samples synthesized under four different conditions were determined using the FESEM. Figure 3d–g shows the FESEM images of $NiFe_2O_4$ nanoparticles, and Fig. 3h–k represents the particle size distribution histograms derived from the FESEM of the respective samples. All the FESEM images showed particles smaller than 100 nm with different morphology for the samples attained from four different conditions. $NiFe_2O_4$ sample prepared under NFO-S conditions, where the sodium hydroxide (NaOH) is the primary precipitant (Fig. 3d), had an average size of 47 nm with mixed rhombohedron morphology. $NiFe_2O_4$ sample prepared under NFO-U conditions, where along with NaOH, urea was used as a co-precipitant and Polyethylene glycol (PEG400) (non-ionic) surfactant was employed (Fig. 3e) showed the smallest average nanoparticle size of 22 nm with a nanosphere-like morphology. From Fig. 3f, the $NiFe_2O_4$ sample prepared under NFO-G conditions showed polyhedron-shaped nanoparticles with an average particle size of 60 nm. $NiFe_2O_4$ sample prepared under NFO-C conditions displayed a morphology of nanocubes with 82 nm average particle size as shown in Fig. 3g.

Varying the additives in the precursor solution might affect both the direction and rate of crystal growth, resulting in different morphologies. NaOH, the common precipitant in all four synthesis conditions, readily provides OH^- ions, which allows metal ions to react easily and initiate nucleation before the hydrothermal reaction. By controlling the pH and molar ratio, we were able to facilitate the anisotropic growth of crystals, leading to the formation of faceted particles of NFO-S, NFO-G, and NFO-C.

In the study of Gao et al., the usage of urea as the only precipitant resulted in nanosheet morphology due to a slow nucleation rate, accredited to the slow release of hydroxyl ions (OH^-) ions upon the pyrolysis of urea [61]. Compared to NFO-S synthesis conditions, in NFO-U, there is abundant flooding of OH^- ions from both NaOH and urea molecules, resulting in rapid nucleation-point due to "multipoint-flowering" conditions in the reactive medium. This ultimately results in the achievement of smaller sized (22 nm) nanoparticles upon nucleation. Subsequently, during the growth phase, the PEG400 gets adsorbed on the surface of the multiple nuclei and influences the growth, resulting in the attainment of nanosphere morphology.

For the NFO-S and NFO-U samples obtained directly from the hydrothermal process, the XRD results confirmed the formation of phase pure inverse spinel structure of $NiFe_2O_4$, and hence, these were not subjected to further calcination. However, for NFO-G and NFO-C, samples obtained directly from the hydrothermal process showed the impurity phases. So, these samples were calcinated at higher temperatures to remove the impurity phases. Hence, $NiFe_2O_4$ samples prepared under glucose (NFO-G) and CTAB (NFO-C) conditions exhibited larger particle sizes, which is due to the calcination effect at a high temperature. Further, it is stated that glucose and CTAB are used to obtain varied morphology of $NiFe_2O_4$ samples.

In NFO-G, the real motivation for the employment of glucose (which was neither a surfactant nor a co-precipitant) molecule along with NaOH was to achieve hollow nanosphere morphology, as seen in the work of Maria-Magdalena Titirici et al., for binary metal oxides [62]. Surprisingly, in our nickel ferrite system, the usage of glucose during the hydrothermal process coupled with the calcination step, effectuated a non-uniform polyhedral morphology with sharp edges and an average size of 60 nm (Fig. 3f).

The successful attainment of different morphologies in nickel ferrite nanoparticles through different synthesis routes is due to two crucial factors: (1)

Influence of alkalinity by the precipitants present in the reaction medium and (2) Guidance of preferential growth of crystalline planes by the surfactants [61, 63]. Thus, to achieve cubical plate-like morphology, cetyltrimethylammonium bromide (CTAB), a cationic surfactant, was employed with NaOH precipitant in NFO-C conditions, as reported by Chengsi Pan et al., in their hydrothermal process for attaining binary cerium oxide nanoplates [63]. Interestingly, we did not observe the phase pure inverse spinel structure of $NiFe_2O_4$ upon the implementation of CTAB in our hydrothermal process, prior to calcination. However, it resulted in nanocube morphology following the calcination step after the hydrothermal reaction. NFO-S, NFO-C, and NFO-G samples have nanopolyhedral structures with flat faces and straight edges, whereas NFO-U sample has spherical nanoparticles with curved surfaces. The elemental distribution in NFO-C is studied using EDX, and the EDX mapping of the NFO-C is given in Figure S2 in Supporting Information. It confirmed the presence and uniform distribution of Ni, Fe, and O elements in NFO-C.

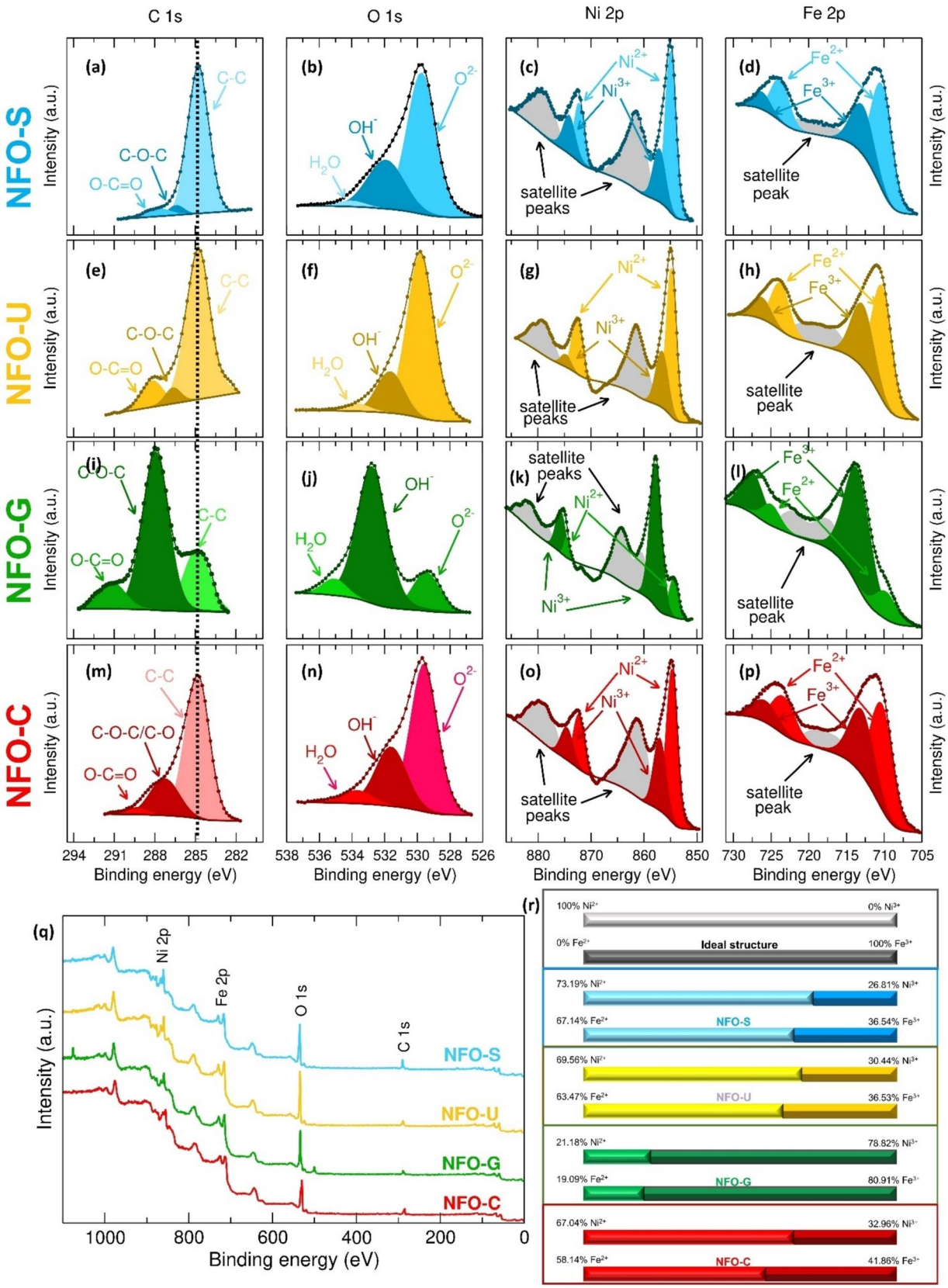
The XRD study confirmed the cubic inverse spinel structure for the different morphologies accomplished for nickel ferrite nanoparticles. The Raman spectroscopy studies reconfirmed the crystal structure but indicated the redistribution of cations in the fcc lattice. At the same time, in the case of pristine NFO-S and NFO-U nanoparticles, there might be a presence of surfactants or pyrolyzed products of surfactants on the surface of nanoparticles, as there was no calcination step involved in their synthesis route. In the case of NFO-G and NFO-C, there might be oxidized products of surfactants on their nanoparticles, as they were subjected to high-temperature treatment in an ambient air-filled muffle furnace setup.

Thus, to understand the surface chemistry of the nanoparticles, valence state, and distribution of cations, the XPS study was carried out in this work. Figure 4 shows C 1s, O 1s, Ni 2p, Fe 2p high-resolution spectra, the XPS survey scan of the four $NiFe_2O_4$ samples, and the corresponding surface cation distribution in these nanoparticles. The surface chemistry of $NiFe_2O_4$ samples helps to evaluate the effect of different morphological influences on the battery performance of nano-$NiFe_2O_4$ as an anode material.

The high-resolution O 1s, Ni 2p, and Fe 2p XPS spectra shown in Fig. 4a–p of the four $NiFe_2O_4$ nanoparticle samples were peak shifted to neutralize the charging effect with respect to 284.8 eV peak of C–C bonding in C 1s spectrum [64]. As the pristine NFO-S nickel ferrite was synthesized without any organic surfactants, the source for C 1s spectrum was carbon contamination during XPS measurements. The deconvolution of this C 1s spectrum in Fig. 4a is necessary to differentiate the carbon contribution coming from the surfactants and from the XPS equipment. Deconvolution of C 1s spectrum in Fig. 4a discloses distinctive sp^3 and sp^2 hybridized carbon peaks: 284.8 eV, 286.4 eV, and 288 eV corresponding to C–C, C–O–C and O–C=O bonds, respectively, arising from adventitious carbon during XPS measurements [65].

The deconvoluted O 1s spectrum of NFO-S consists of three peaks at 529.7 eV, 531.9 eV, and 534 eV ascribed to lattice oxygen O^{2-} bonded to metal ions (Ni^{2+} and Fe^{3+}), hydroxyl group OH^-, and absorbed water molecule on the surface, respectively (Fig. 4b) [66]. Figure 4c shows the high-resolution XPS spectrum of Ni 2p, which involves major peaks at 855 eV and 872.5 eV (Ni $2p_{3/2}$ and Ni $2p_{1/2}$) due to spin–orbit coupling followed by their shake-up satellite peaks at 861.5 eV and 880 eV. Ni $2p_{3/2}$ and Ni $2p_{1/2}$ core levels can be further deconvoluted into Ni^{2+} and Ni^{3+}. In Fig. 4c, the fitted peaks within the Ni 2p spectrum, at the binding energy of 854.9 eV and 872.2 eV, correspond to Ni^{2+}, whereas 857.11 eV and 874.13 eV correspond to Ni^{3+} [66]. Concurrently, the Ni 2p spectrum (Fig. 4c) exhibits an asymmetric shape for NFO-S nickel ferrite nanoparticles, indicating the presence of two non-equivalent bonds of Ni ions, present both in the tetrahedral and octahedral lattice sites of the spinel structure [55]. This confirms the redistribution of cations within the spinel structure, as observed in the Raman spectroscopy measurement in Fig. 3c. This asymmetric shape is evident in the Ni 2p spectra of all four $NiFe_2O_4$ nanoparticle samples analyzed in Fig. 4.

In the case of pristine NFO-S nanoparticles, unlike the idealistic bulk $NiFe_2O_4$ material, the surface of $NiFe_2O_4$ contains Ni^{3+} in addition to Ni^{2+} and their corresponding (Ni^{3+}/Ni^{2+}) ratio is 0.36. Similarly, the Fe 2p high-resolution spectrum of NFO-S (Fig. 4d) has Fe $2p_{3/2}$ and Fe $2p_{1/2}$ peaks at 710.5 and 723.9 eV followed by satellite peaks, and the deconvolution of these peaks gives the Fe^{2+} and Fe^{3+} peaks. Specifically, the fitted peaks of the Fe 2p spectrum in Fig. 4d, at 710.28 eV and 723.8 eV correspond to Fe^{2+} and peaks at 712.9 eV and 726.29 correspond to Fe^{3+}[66, 67]. The (Fe^{3+}/Fe^{2+}) ratio in NFO-S nanoparticles is 0.544. The additional Ni^{3+}, Fe^{2+}, and OH^- peaks are indicative of the presence of possible supplementary compositions


C 1s
O 1s
Ni 2p
Fe 2p
NFO-S
NFO-U
NFO-G
NFO-C
Intensity (a.u.)
(a)
C-C
C-O-C
O-C=O
(b)
O2-
OH-
H2O
(c)
Ni2+
Ni3+
satellite peaks
(d)
Fe2+
Fe3+
satellite peak
(e)
(f)
(g)
(h)
(i)
(j)
(k)
(l)
(m)
C-O-C/C-O
(n)
(o)
(p)
294 291 288 285 282
538 536 534 532 530 528 526
880 870 860 850
730 725 720 715 710 705
Binding energy (eV)
(q)
Ni 2p
Fe 2p
O 1s
C 1s
1000 800 600 400 200 0
(r)
100% Ni2+
0% Ni3+
0% Fe2+
Ideal structure
100% Fe3+
73.19% Ni2+
26.81% Ni3+
67.14% Fe2+
36.54% Fe3+
69.56% Ni2+
30.44% Ni3+
63.47% Fe2+
36.53% Fe3+
21.18% Ni2+
78.82% Ni3+
19.09% Fe2+
80.91% Fe3+
67.04% Ni2+
32.96% Ni3+
58.14% Fe2+
41.86% Fe3+

◂**Fig. 4** XPS high-resolution spectra of C 1s, O 1s, Ni 2p and Fe 2p of **a**–**d** NFO-S, **e**–**h** NFO-U, **i**–**l** NFO-G and **m**–**p** NFO-C, **q** Survey spectra of the four nickel ferrite nanoparticle samples and **r** Percentage of different valence states of Ni and Fe ions present on the four $NiFe_2O_4$ samples estimated through XPS

on the surface of $NiFe_2O_4$ nanoparticles. During the synthesis of NFO-S samples, the sole basic precipitant (NaOH) provides excess OH^- ions, and NiO(OH) and $Fe(OH)_2$ might have formed at the surface. Along with $NiFe_2O_4$, there might be FeO, which gives rise to the Fe^{2+} oxidation state; however, Ni_2O_3 might not be present because of its unstable nature [68, 69].

Unlike NFO-S, other samples have co-precipitants and/or surfactants in their synthesis procedure, which is also reflected in their XPS spectra. In Fig. 4e, the deconvoluted C 1s spectrum of NFO-U contains more proportions of C–O–C and O–C=O bonds in addition to the carbon contaminations from XPS. In NFO-U synthesis, the decomposition of urea during hydrothermal reaction at 200 °C, along with the presence of OH^-, could have resulted in the formation of –COOH carboxyl groups that have potentially coated on the surface of the NFO-U nanoparticles. Formation of the carboxyl group has resulted in the decrement of metal-hydroxide formation, which explains the reason for the lower intensity deconvoluted OH^- peak in the O1s spectrum of NFO-U (Fig. 4f), compared to NFO-S. The Ni 2p and Fe 2p spectra of NFO-U (Figs. 4g and h) are almost similar to that of NFO-S (Figs. 4c and d). On the surface of NFO-U, the ratio of Ni^{3+}/Ni^{2+} and Fe^{3+}/Fe^{2+} obtained from the corresponding peaks are 0.44 and 0.58, respectively. In NFO-G, the deconvoluted C 1s spectrum (Fig. 4i) contains a larger C–O–C peak in addition to carbon contamination peaks. This could have been attributed to the trace amount of contamination products from the pyrolysis of glucose present along with precursors of NFO-G nanoparticles. A prominent OH^- peak larger than the lattice oxygen peak is visible in the O 1s spectrum of NFO-G (Fig. 4j). Upon the completion of the hydrothermal process in NFO-G synthesis, the surface of $NiFe_2O_4$ may be coated with products from decomposition of glucose and calcination of such complex at higher temperatures in the ambient environment may result in the formation of metal-hydroxide bonds on the surface of NFO-G nanoparticles. This explains the reason for the higher intensity OH^- compared to the lattice metal–oxygen peak. Even though, in the Ni 2p and Fe 2p spectra of NFO-G (Figs. 4k and l), deconvolution peaks are similar to NFO-S and NFO-U without any additional components, Ni^{3+} and Fe^{3+} peaks are considerably higher compared to other samples. Subsequently, the ratio of surface cation distribution is 3.72 and 4.26 for Ni^{3+}/Ni^{2+} and Fe^{3+}/Fe^{2+}. As both the precipitant NaOH and glucose provide excess amount of OH^- ions upon decomposition, it eventually triggers the formation of higher proportion of NiO(OH) and FeOOH, explaining the rationale for the increased ratios of Ni^{3+}/Ni^{2+} and Fe^{3+}/Fe^{2+}.

The C 1s spectrum of NFO-C (Fig. 4m) shows peaks from the carbon contamination molecules from XPS equipment and C–O group. Decomposition of CTAB surfactant during calcination step at 500 °C in ambient atmosphere is potential reason for the occurrence of C–O bonding on the surface of NFO-C nanoparticles. The O 1s spectrum of NFO-C (Fig. 4n) is similar to that of the NFO-S, containing lattice oxygen, hydroxyl group, and absorbed water molecule peaks. Ni 2p and Fe 2p spectra of NFO-C (Figs. 4o and p) are similar to NFO-S (Figs. 4c and d) showing that the similar additional chemical compositions (NiO(OH) and $Fe(OH)_2$) present on the surface of NFO-C. The Ni^{3+}/Ni^{2+} and Fe^{3+}/Fe^{2+} ratios at surface of NFO-C are 0.49 and 0.72, respectively.

Figure 5a shows the nitrogen adsorption–desorption isotherms of $NiFe_2O_4$ samples prepared under four different conditions. The surface areas of each sample were calculated from BET analysis, and it was found to be 65.7 m^2/g, 40.8 m^2/g, 18.7 m^2/g, and 16.13 m^2/g for $NiFe_2O_4$ samples prepared under NFO-U, NFO-S, NFO-G, and NFO-C conditions, respectively. Figure 5a inset shows the pore size distribution of $NiFe_2O_4$ samples prepared under four different conditions. The surface area and the cumulative pore volumes calculated from N_2 adsorption–desorption curves are presented in Table 2.

From Fig. 5a, the N_2 adsorption and desorption spectra, the NFO-S, NFO-G, and NFO-C show type-IV, H3-hysteresis loops, and NFO-U shows a type-IV, H2(b)-hysteresis loop. The type-IV hysteresis loop indicates that the pores present are of mesoporous nature. At lower pressure, the adsorption logarithmically increases and leads to a linear increase in the mid-section, which corresponds to the monolayer filling and starting of multilayer adsorption. The hysteresis nature of the graph is associated with the capillary condensation in mesopores [70–73]. NFO-U's H2-type hysteresis loop is attributed to the ink-bottle-shaped

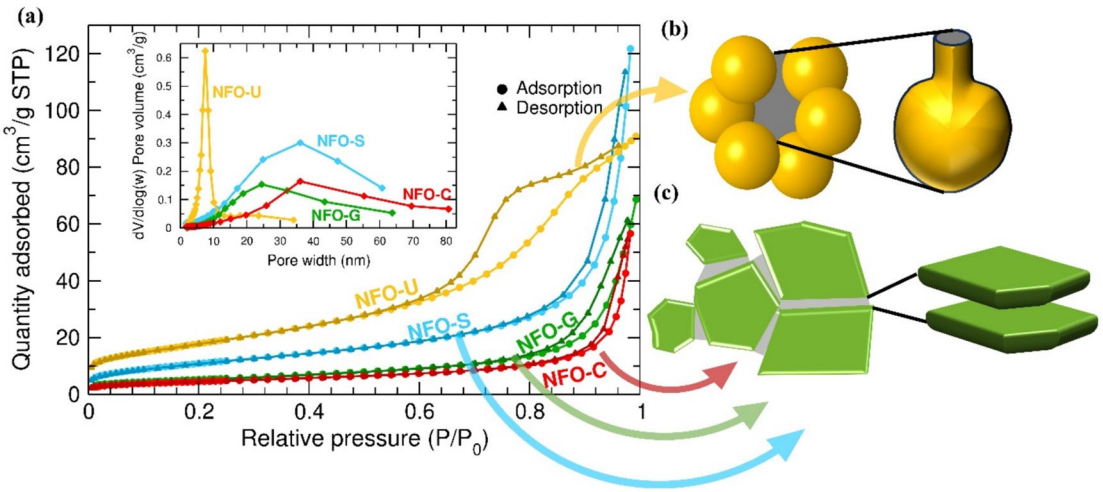


Fig. 5 **a** N_2 adsorption and desorption isotherms and (inset) pore size distribution of $NiFe_2O_4$ samples. Schematic representation of **b** ink-bottle type pore and **c** slit-shaped pore

Table 2 Surface area and Pore volume of NFO-S, NFO-U, NFO-G, and NFO-C

	Surface area (m^2/g)	Cumulative pore volume (cm^3/g)	
		Adsorption	Desorption
NFO-S	40.8	0.189	0.190
NFO-U	65.7	0.142	0.145
NFO-G	18.7	0.106	0.107
NFO-C	16.1	0.087	0.087

pore structure with a narrow neck region and wide body region possessing a volume in the range of 0.142–0.145 cm^3/g, as illustrated in Fig. 5b. H3-hysteresis loops of the remaining three nickel ferrite nanoparticles depict that they are mesoporous in nature with the slit-shaped pore structure, as shown in Fig. 5c.

From the inset of Fig. 5a presenting the pore size distribution, the mesoporous nature of $NiFe_2O_4$ samples is reconfirmed as the effective pore width is within the range of 2 to 50 nm. The NFO-U sample has a sharp peak in the pore distribution curve at 7.5 nm and has the smallest effective pore width. NFO-S, NFO-G, and NFO-C samples have broadened pore distribution graphs. NFO-S and NFO-C have the highest and comparable effective pore width. However, NFO-S has the highest pore volume, and NFO-C has the lowest.

The BET hysteresis curve and FESEM data can be compared to analyze the pore morphology of the four $NiFe_2O_4$ nanoparticle samples. NFO-U nanoparticles exhibit roughly a nanosphere morphology with highly curved surfaces (Fig. 3e), and they aggregate to form the ink-bottle-shaped pore structure (Fig. 5b). From the FESEM data, NFO-S, NFO-G, and NFO-C have flat surfaces with sharp edges (Figs. 3d, f, and g), and their agglomeration results in slit-like pores, which are confirmed by the H3-type hysteresis graph. This is pictorially represented in Fig. 5c. Also, the particle size of $NiFe_2O_4$ nanoparticles from FESEM images can be compared with the surface area found in BET. The NFO-U $NiFe_2O_4$ sample, with the smallest average particle size (22 nm), has the largest surface area, and NFO-S with an average particle size of 47 nm, exhibits the 2nd largest surface area. NFO-G (60 nm) and NFO-C (82 nm), with larger particle sizes, have a lower surface area than NFO-U and NFO-S, due to the calcination step involved in their synthesis condition. NFO-C, with the larger particle size, shows a smaller surface area than the NFO-G sample.

Figure 6a–d shows the cyclic voltammetry (CV) results of $NiFe_2O_4$ nanoparticles synthesized under four different conditions for 5 cycles. The first discharge curve corresponds to the reduction of $NiFe_2O_4$ to nickel (Ni) and iron (Fe). Equation 6 represents the first lithiation step, where lithium (Li) gets oxidized by supplying electrons to $NiFe_2O_4$, and lithium oxide (Li_2O) is formed during this reaction.

$$NiFe_2O_4 + 8Li^+ + 8e^- \rightarrow 4Li_2O + Ni + 2Fe. \quad (6)$$

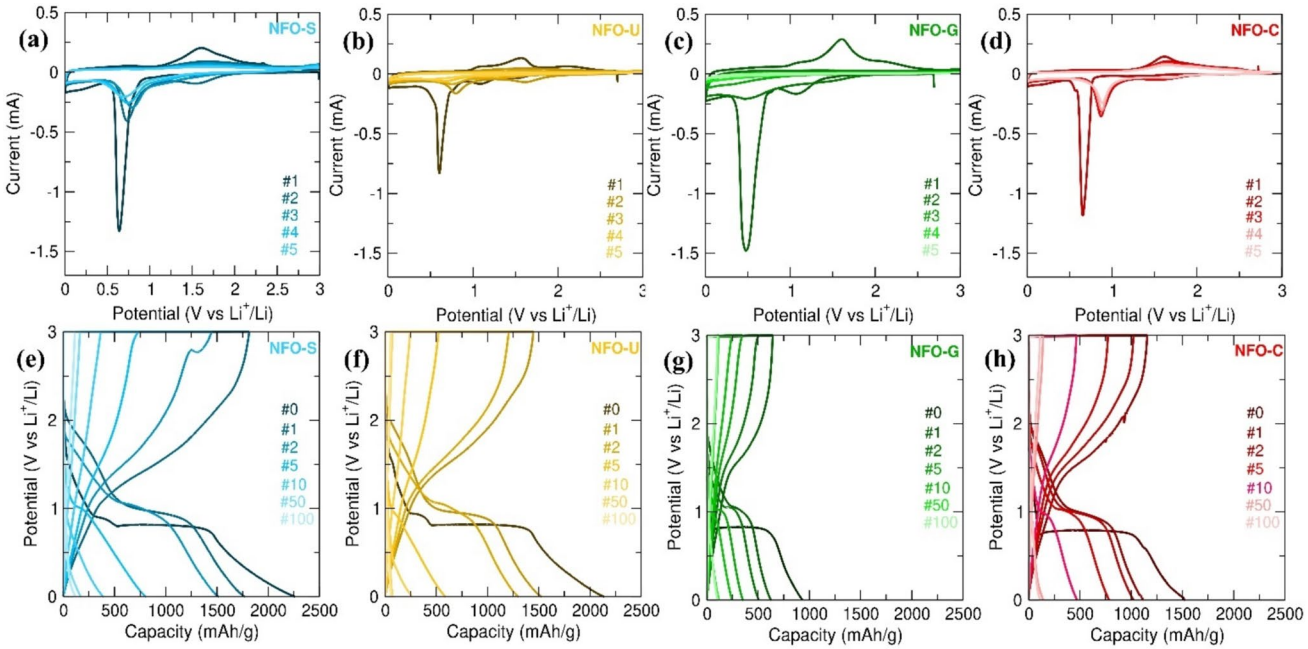


Fig. 6 **a–d** Cyclic voltammetry and **e–h** galvanostatic charge–discharge of NFO-S, NFO-U, NFO-G and NFO-C, respectively

During charging, the peak in the anodic scan corresponds to the oxidation of metal ions, as given in Eq. 7, and Li_2O gets reduced by accepting the electron. Fe ions get converted to Fe_2O_3 completely, whereas only a fraction of Ni metal gets oxidized to NiO [74]. This can be clearly observed from the depletion of the reduction peak from the first cycle to the second cycle.

$$4Li_2O + Ni + 2Fe \leftrightarrow (1 - x)NiO + xNi + Fe_2O_3 + xLi_2O + (8 - 2x)\left(Li^+ + e^-\right) \quad (7)$$

$(0 < x < 1)$.

Equation (6) is irreversible, whereas Eq. (7) is reversible. The shift of the reduction peaks after the first cycle shows the irreversibility and the low-capacity retention of the anode materials [2, 31, 74].

Comparing the four CV graphs, NFO-C shows the best retention where reduction (except 1st cycle) and oxidation peaks are at around the same voltage 0.86 V and 1.62 V, respectively, with lesser change in the peak height, whereas NFO-G and NFO-U show the poorest retention and the peaks disappear by the 5th cycle. NFO-S shows moderate capacity retention with the fluctuating reduction peak voltage.

Figure 6e–h shows the charge–discharge profiles of $NiFe_2O_4$ nanoparticles synthesized under conditions of NFO-S, NFO-U, NFO-G, and NFO-C, respectively, between voltage range of 0.01–3 V (vs Li/Li^+) at a constant current density of 100 mA/g. In the initial discharge curve, all samples show a plateau region near 0.8 V, different from other consecutive cycles. This plateau region resembles the sharp peak in the first cathodic sweep of CV, indicating the irreversible reduction of $NiFe_2O_4$ to Ni and Fe and the formation of Li_2O [74].

NFO-S delivers an initial discharge capacity of 2258 mAh/g, and NFO-U gives the next highest discharge capacity of 2136 mAh/g. NFO-C and NFO-G have initial discharge capacities of 1523 and 934 mAh/g, respectively. First charge capacity also follows the same trend in the order of NFO-S, NFO-U, NFO-C, and NFO-G with capacities of 1815, 1446, 1156, and 643 mAh/g, respectively. After 100 cycles, NFO-S gives the highest discharge capacity of 116 mAh/g, whereas the discharge capacity of NFO-C and NFO-G comes near to the capacity displayed by NFO-S after 100 cycles, which are 112 and 106 mAh/g, respectively. However, the sample NFO-U with the second highest initial capacity drops to the lowest discharge capacity, 56 mAh/g, after 100 cycles. Table 3 tabulates the first discharge and

Table 3 First discharge and charge capacity and 100th discharge capacity of $NiFe_2O_4$ samples

Samples	NFO-S	NFO-U	NFO-G	NFO-C
1st discharge capacity (mAh/g)	2258.88	2136.21	934.44	1523.25
1st charge capacity (mAh/g)	1815.42	1446.84	643.11	1156.32
100th discharge capacity (mAh/g)	116.33	56.50	106.52	112.68

charge capacities and the 100th discharge capacities of NFO-S, NFO-U, NFO-G, and NFO-C.

Figure 7a–c shows the plots of charge capacity, discharge capacity, and coulombic efficiency vs cycle number of $NiFe_2O_4$ nanoparticles synthesized under four different synthesis conditions. The discharge and charge capacities of nickel ferrites follow a similar trend throughout the cycles. NFO-S dominates in specific capacities over most of the cycles except from the 6th to 17th cycle. NFO-U, with the second highest initial capacity, falls to the lowest capacity range by the 15th cycle. A poor capacity retention is observed for all the $NiFe_2O_4$ sample in Fig. 7a and b, and the key reasons are their poor conductivity and volume expansion during cycling. The surface area and particle size of anode materials directly influence the performance of LIBs [7, 75, 76]. $NiFe_2O_4$ nanoparticles (both NFO-S and NFO-U) with the lowest particle size and large surface area have high initial discharge and charge capacities. The larger surface area provides more sites for lithiation; hence, the capacity increases [51].

From Fig. 7c, the NFO-G and NFO-C samples, having larger particle sizes and lower surface area showed a higher coulombic efficiency compared to the NFO-S and NFO-U samples, having small particle sizes and higher surface area. In NFO-S and NFO-U samples, the observed higher surface area may increase the electrode–electrolyte interface, which in turn increases the electrolyte decomposition on the electrode surface and leads to the formation of the solid electrolyte interphase (SEI) layer [77]. However, the formation of an excess SEI layer may offer higher resistance to the Li-ion diffusion, which in turn reduces the reversibility of lithium ions and results in lower coulombic efficiency [78, 79]. In NFO-G and NFO-C samples, the observed lower surface area may decrease the electrode–electrolyte interface, which in turn results in less or optimum decomposition of electrolyte and may form a more stable and uniform SEI layer. This may reduce the lithium loss and enhance the charge transfer, increasing the cyclic stability and leading to a higher coulombic efficiency.

Even though the NFO-U sample has a smaller particle size and higher surface area compared to NFO-S, it exhibits lower discharge capacity and reduced capacity retention. The key reason for the exhibiting lower discharge capacity of NFO-U may be due to the formation of the ink-bottle-shaped pore structure, which is confirmed by the BET results (Fig. 5). The ink-bottle-shaped pores of NFO-U with a narrow entrance and wider interior may restrict the diffusion of Li ions by limiting access to inner pore surfaces, reducing the utilization of active sites inside the pores, resulting in low specific capacity (Fig. 5b). The slit-shaped pores of

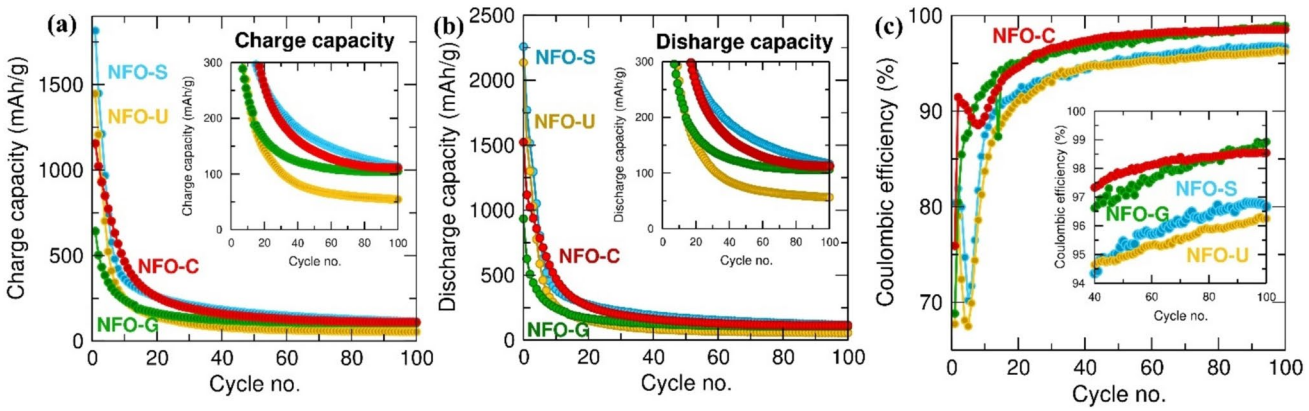


Fig. 7 Plots of **a** charge capacity, **b** discharge capacity and **c** coulombic efficiency vs. cycle number during charge–discharge at a current density of 100 mA/g for 100 cycles

NFO-S may provide more accessible pathways for Li-ion transport, maximizing the utilization of the active sites resulting in high specific capacity (Fig. 5c). Hence, the NFO-U exhibited lower discharge capacity even though it has a higher surface area, compared to NFO-S. The highly defective performance of NFO-G could be attributed to the presence of supplementary compositions (contaminations) from their synthesis route potentially due to the decomposition of glucose molecules, as observed from NFOG's XPS spectra (Figs. 4i, j, k, and l).

Comparing all four $NiFe_2O_4$ samples prepared under four different conditions, NFO-S shows the best lithium storage capacity, and NFO-C shows the best coulombic efficiency over 100 cycles. The higher charge and discharge capacities of NFO-S compared to all other samples can be attributed to its large surface area, pore volume, and slit-shaped pores, as it provides more active sites for lithiation regardless of its low coulombic efficiency [80]. So, the optimization of the surface area of $NiFe_2O_4$ nanoparticles can offer good capacity with cyclic stability. Concurrently, the morphology, surface chemistry of nanoparticles, interparticle voids, and the porous nature of the $NiFe_2O_4$ samples have a great influence on lithium diffusion and electrochemical performance. We have also systematically compared the electrochemical performance of the best $NiFe_2O_4$ anode (NFO-S) studied in this work with the $NiFe_2O_4$ anode materials reported so far in the literature, in Table S2 of the Supporting Information.

Figures 8a, b, c, and d presents the Nyquist plots (Re(Z) vs -Im(Z)) from electrochemical impedance spectroscopy (EIS) of Li-ion half-cells, fabricated using the $NiFe_2O_4$ nanoparticles synthesized under four different conditions as anode materials, before cycling and after 100 cycles. EIS helps us to understand the complex electrochemical reactions inside the cell, including lithium-ion migration through the liquid electrolyte, charge transfer inside the active materials, and conduction through the SEI layer. Due to the distinct relaxation times of these different processes, the cell responds uniquely to each of the activities when the frequency is varied. Unlike the ideal situation, the spectrum does not provide separate features for each electrochemical activity, and the Nyquist graph analysis using an equivalent electrical circuit simplifies the study. The Randles circuit is the highly preferred and uncomplicated equivalent circuit to study the EIS data of lithium-ion half-cells fabricated with metal oxide as electrode material [81]. The fitting of the Randles circuit for our EIS data gave a very low χ^2 value (in the range of 10^{-3}); see Table S1 from the Supporting information.

Figure 8e and f shows the equivalent circuit model for the Li-ion half-cell with nickel ferrite as the working electrode before cycling and after 100 cycles, respectively. The Nyquist plot in Figs. 8a, b, c and d comes with a semicircle followed by an inclined line, which can be divided into high, mid, and low-frequency ranges. R_{el} is the resistance of electrolyte towards the ions, and it is found from the x-intercept of the Nyquist plot at high-frequency range. The mid-frequency range consists of a charge transfer mechanism (electrons and ions), double-layer charging at the anode and reactions at the SEI layer. R_{ct} is the charge transfer resistance of redox reactions and Q_{dl} is the constant phase element (CPE) for double-layer capacitance at the active material. R_{SEI} and Q_{SEI} represent the ohmic resistance of Li^+ ion at the SEI layer and SEI layer capacitance, respectively. At lower frequencies, diffusion of Li^+ ions occurs and is indicated by the Warburg impedance (W) of the electrode. The constant phase element, which is in series with Warburg impedance, Q_{int} represents the low-frequency bulk capacitance. The diameter of the depressed semicircle is the sum of charge transfer resistance (R_{ct}) and SEI layer resistance (R_{SEI}), and the inclined straight line relates to Warburg impedance [82–85].

The calculated values for R_{el}, R_{ct}, and R_{SEI} obtained from the equivalent circuit are given in Table 4. The R_{el} values of $NiFe_2O_4$ samples do not show much difference before and after cycling except for NFO-C. Compared to the R_{ct} values prior to the first cycle, it has been substantially increased for all the $NiFe_2O_4$ samples after 100 cycles of charge–discharge. The significant increase in resistive elements validates the capacity decline for our samples over 100 cycles.

The Li^+ ion diffusion coefficient is calculated using the following Eq. (8) where R is the Ideal gas constant, T is temperature, A is the area of the electrode, n is the number of electrons transferred, F is the Faraday Constant, C is the concentration of active species, and σ is Warburg coefficient calculated from EIS data and tabulated in Table 5.

$$D_{Li^+} = \frac{R^2T^2}{2A^2n^4F^4C^2\sigma^2}(\mathrm{cm}^2/\mathrm{s}) \quad (8)$$

The lithium diffusion coefficients of NFO samples decrease after 100 cycles, indicating an increase in

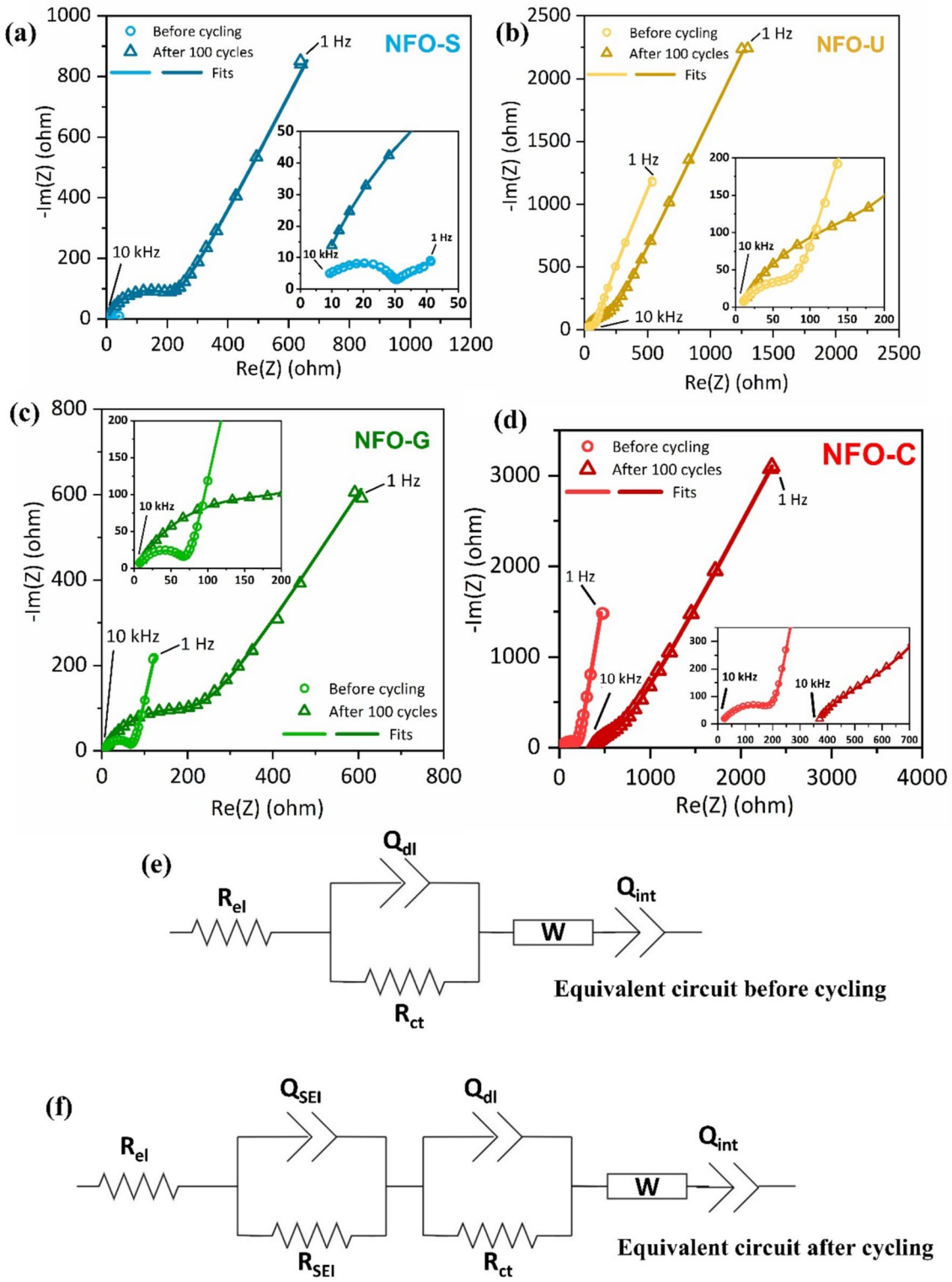


Fig. 8 Nyquist plots of **a** NFO-S, **b** NFO-U, **c** NFO-G, **d** NFO-C before cycling and after 100 cycles and equivalent circuit model for the half-cell fabricated with $NiFe_2O_4$ anode **e** before cycling and **f** after 100 cycles

Table 4 Electrolyte resistance, Charge transfer resistance, and SEI layer resistance values calculated from EIS of NFO-S, NFO-U, NFO-G, and NFO-C

Material		R_{el} (Ω)	R_{ct} (Ω)	R_{SEI} (Ω)
NFO-S	Before 1st Cycle	5.622	23.51	–
	After 100 cycles	4.385	208.4	14.53
NFO-U	Before 1st Cycle	7.902	117.2	–
	After 100 cycles	9.007	190.9	1.416
NFO-G	Before 1st Cycle	4.076	67.61	–
	After 100 cycles	4.941	197.5	0.298
NFO-C	Before 1st Cycle	12.16	200	–
	After 100 cycles	341.9	253.9	0.455

Table 5 Li^+ ion diffusion coefficient values obtained from EIS of NFO-S, NFO-U, NFO-G and NFO-C

Material	Li^+ ion diffusion coefficient (cm^2/s)	
	Before 1st cycle	After 100 cycles
NFO-S	1.303×10^{-10}	9.020×10^{-14}
NFO-U	1.098×10^{-13}	2.119×10^{-14}
NFO-G	3.217×10^{-13}	5.252×10^{-15}
NFO-C	2.012×10^{-13}	6.066×10^{-15}

internal resistance reflected in capacity loss. Before cycling, NFO-S exhibited the highest lithium diffusion coefficient, leading to an excellent first discharge capacity.

The sample NFO-S with the highest pore volume (0.190 cm^3/g) shows the lowest charge transfer resistance (23.51 Ω) and also exhibits the highest specific capacity (2258.88 mAh/g). As the BJH cumulative pore volume and BET surface area increase (Table 2), the charge transfer resistance decreases, except for NFO-U. The distinctive behavior of NFO-U can be explained by its ink-bottle-shaped pore structure. The bottleneck pore entrance decreases the Li^+ ion diffusion. Hence, the charge transfer resistance increases in the case of NFO-U.

The specific capacity of $NiFe_2O_4$ nanoparticles is not solely dependent on charge transfer resistance, which in turn is influenced by the surface area and morphology of the nanoparticle pore structure, as seen in the case of NFO-S and NFO-U. However, it is also influenced by the surface chemistry and cation distribution within the spinel structure of crystalline $NiFe_2O_4$ nanoparticles. This is evident in the case of NFO-G and NFO-C materials. Here, even though NFO-C has the lowest pore volume (0.087 cm^3/g) and surface area (16.13 m^2/g) with the highest charge transfer resistance (200 Ω), it still exhibits higher specific capacity (1523.25 mAh/g) than NFO-G nanoparticle (934.44 mAh/g), with higher surface area (18.7 m^2/g), high pore volume (0.107 cm^3/g), and low charge transfer resistance (67.61 Ω).

Figure S3 in Supporting Information shows the rate performance of NFO-S, NFO-G, and NFO-C cycled for 10 cycles at each current densities: 50 mA/g, 100 mA/g, 500 mA/g, 1 A/g, 2 A/g, 5 A/g, 10 A/g, and 20 A/g. The $NiFe_2O_4$ prepared under NFO-S condition showed a superior rate performance over other samples. NFO-S exhibited a good rate performance with an average discharge capacity of 106 mAh/g at 1 A/g current density, and it retained an average discharge capacity of 515 mAh/g at a current density of 50 mA/g after the cycling at a higher current density of 20 A/g. NFO-U was not able to be studied for the rate performance due to its poor cyclic retention and very low capacity at higher current densities.

All in all, this study clearly points out that an optimum balance between the surface area, morphology, porosity, surface chemistry, and cationic distribution within the spinel structure is required for achieving higher electrochemical performance for LIBs using $NiFe_2O_4$ as an anode material. The $NiFe_2O_4$ sample prepared under NFO-S condition exhibited higher specific capacity compared to the other three samples. The higher capacity of the NFO-S sample can be attributed to its high surface area with slit-like pore structure, which resulted from the agglomeration of rhombohedral-shaped nanoparticles, whereas the $NiFe_2O_4$ sample prepared under the NFO-C condition showed good cyclic stability over others, which is attributed to the stable SEI layer formation as a result of its lower surface area. These samples with superior performance over others will be taken for further studies including compositing with conductive carbon materials like CNT, graphene, and its derivatives with porous structure and high surface area to improve the conductivity and cyclic performance by reducing the volume expansion [46, 47].

4 Conclusions

$NiFe_2O_4$ nanoparticles were synthesized through the hydrothermal route under four different conditions. The phase purity, morphology, particle size, and surface chemistry of the $NiFe_2O_4$ samples synthesized

under different conditions were studied using XRD, FTIR, Raman spectroscopy, FESEM, XPS, and BET. The $NiFe_2O_4$ nanoparticle sample prepared with NaOH precipitant without any surfactants (NFO-S) exhibited a higher initial discharge capacity of 2258 mAh/g and a higher initial charge capacity of 1815 mAh/g at a current density of 100 mA/g, compared to the other three samples. The $NiFe_2O_4$ sample prepared with CTAB (NFO-C) showed better cyclic stability with good coulombic efficiency over 100 cycles. CV results of the NFO-S and NFO-C samples showed more stable and reversible conversion reactions compared to other samples, which is attributed to their morphology, surface area, porosity, and surface chemistry. In conclusion, the $NiFe_2O_4$ samples synthesized under NFO-S and NFO-C conditions exhibited better lithium storage performance, showing high specific capacity and cyclic stability, respectively, due to their individual morphology and surface properties. This work provides guidance on the effect of hydrothermal synthesis conditions on the electrochemical performance of $NiFe_2O_4$ nanoparticles, focusing on their morphology and surface properties. This work also paves the way for future research to develop high-performing $NiFe_2O_4$ composite anode materials incorporating advanced conductive materials with large surface areas such as carbon nanotubes (CNT), graphene, MXenes, transition metal dichalcogenides (TMDs), etc.

Acknowledgements

R.S.B. is grateful to CSIR, Govt of India for CSIR-SRF Fellowship (No. 09/559(0158)/2020-EMR-I). N.S. acknowledges UGC, Govt of India for awarding UGC-BSR Faculty Fellowship (No. F.18-1/2011(BSR), Date: 07-03-2019). R.S.B. is grateful to the Central Instrumentation Facility (CIF), Pondicherry University for utilizing the characterization facilities.

Author contributions

RSB: Conceptualization, Methodology, Validation, Investigation, Data Curation, Writing—Original Draft, Visualization; EM: Visualization; DSN: Data Curation; PG: Data Curation, Supervision, Writing—Review & Editing; SMA: Data Curation; RH: Data Curation; TP: Resources, Methodology, Validation; RM: Resources, Writing—Review & Editing; VVRKK: Resources, Writing—Review & Editing; PT: Resources, Writing—Review & Editing AM: Resources, Writing—Review & Editing; NS: Conceptualization, Methodology, Resources, Writing—Review & Editing, Supervision, Project administration, Funding acquisition; PRA: Supervision, Conceptualization, Resources, Data Curation, Writing—Review & Editing.

Funding

R.S.B. has received research support from CSIR, Govt of India through CSIR-SRF Fellowship (No. 09/559(0158)/2020-EMR-I). N.S. has received UGC-BSR Faculty Fellowship support from the UGC, Government of India (No. F.18-1/2011(BSR), Date: 07-03-2019).

Data availability

Data will be made available on request.

Declarations

Competing interests The authors have no relevant financial or non-financial interests to disclose.

Supplementary Information The online version contains supplementary material available at https://doi.org/10.1007/s10854-025-14886-w.

Open Access This article is licensed under a Creative Commons Attribution 4.0 International License, which permits use, sharing, adaptation, distribution and reproduction in any medium or format, as long as you give appropriate credit to the original author(s) and the source, provide a link to the Creative Commons licence, and indicate if changes were made. The images or other third party material in this article are included in the article's Creative Commons licence, unless indicated otherwise in a credit line to the material. If material is not included in the article's Creative Commons licence and your intended use is not permitted by statutory regulation or exceeds the

permitted use, you will need to obtain permission directly from the copyright holder. To view a copy of this licence, visit http://creativecommons.org/licenses/by/4.0/.

References

1. G. Huang, X. Du, F. Zhang, D. Yin, L. Wang, A facile molten-salt route for large-scale synthesis of $NiFe_2O_4$ nanoplates with enhanced lithium storage capability. Chem. Eur. J. **21**, 14140–14145 (2015). https://doi.org/10.1002/chem.201500910
2. C.T. Cherian, J. Sundaramurthy, M.V. Reddy, P. Suresh Kumar, K. Mani, D. Pliszka, C.H. Sow, S. Ramakrishna, B.V.R. Chowdari, Morphologically robust $NiFe_2O_4$ nanofibers as high capacity Li-Ion battery anode material. ACS Appl. Mater. Interfaces **5**, 9957–9963 (2013). https://doi.org/10.1021/am401779p
3. N. Wang, H. Xu, L. Chen, X. Gu, J. Yang, Y. Qian, A general approach for MFe_2O_4 (M = Zn Co, Ni) nanorods and their high performance as anode materials for lithium ion batteries. J. Power. Sources **247**, 163–169 (2014). https://doi.org/10.1016/j.jpowsour.2013.08.109
4. S. Dai, X. Tang, X. Li, J. Zhang, Z. Shao, Synthesis of $NiFe_2O_4$ with different precipitation agents for Li-ion battery anode material by co-precipitation. J. Solid State Electrochem. **26**, 1211–1220 (2022). https://doi.org/10.1007/s10008-022-05158-2
5. J. Wang, G. Yang, L. Wang, W. Yan, Synthesis of one-dimensional $NiFe_2O_4$ nanostructures: tunable morphology and high-performance anode materials for Li ion batteries. J. Mater. Chem. A **4**, 8620–8629 (2016). https://doi.org/10.1039/c6ta02655a
6. L. Liu, L. Sun, J. Liu, X. Xiao, Z. Hu, X. Cao, B. Wang, X. Liu, Enhancing the electrochemical properties of $NiFe_2O_4$ anode for lithium ion battery through a simple hydrogenation modification. Int. J. Hydrogen Energy **39**, 11258–11266 (2014). https://doi.org/10.1016/j.ijhydene.2014.05.093
7. P. Poizot, S. Laruelle, S. Grugeon, L. Dupont, J.-M. Tarascon, Nano-sized transition-metal oxides as negative-electrode materials for lithium-ion batteries. Nature **407**, 496–499 (2000). https://doi.org/10.1038/35035045
8. X.L. Wang, E.M. Kim, T.G. Senthamaraikannan, D.H. Lim, S.M. Jeong, Porous hollow high entropy metal oxides $(NiCoCuFeMg)_3O_4$ nanofiber anode for high-performance lithium-ion batteries. Chem. Eng. J. (2024). https://doi.org/10.1016/j.cej.2024.149509
9. P. Lavela, J.L. Tirado, $CoFe_2O_4$ and $NiFe_2O_4$ synthesized by sol-gel procedures for their use as anode materials for Li ion batteries. J. Power. Sources **172**, 379–387 (2007). https://doi.org/10.1016/j.jpowsour.2007.07.055
10. C. Vidal-Abarca, P. Lavela, J.L. Tirado, The origin of capacity fading in $NiFe_2O_4$ conversion electrodes for lithium ion batteries unfolded by 57Fe Mössbauer spectroscopy. J. Phys. Chem. C **114**, 12828–12832 (2010). https://doi.org/10.1021/jp103888a
11. J.G. Kim, Y. Noh, Y. Kim, S. Lee, W.B. Kim, Formation of ordered macroporous $ZnFe_2O_4$ anode materials for highly reversible lithium storage. Chem. Eng. J. **372**, 363–372 (2019). https://doi.org/10.1016/j.cej.2019.04.151
12. C. Zhang, C. Jin, G. Teng, Y. Gu, W. Ma, Controllable synthesis of hollow $MnFe_2O_4$ by self-etching and its application in high-performance anode for lithium-ion batteries. Chem. Eng. J. **365**, 121–131 (2019). https://doi.org/10.1016/j.cej.2019.02.004
13. P.R. Anusuyadevi, S. Pranavi, R.N.R. Shaw, E. Mádai, D.J.P. Kumar, P. Gonugunta, P. Taheri, A. Mol, An overview of emerging 2D nanomaterials: general synthesis methods and properties, in *Next-Generation 2D Nanomaterials for Sustainable Energy and Environment-Oriented Applications*. (Royal Society of Chemistry, London, 2025), pp.1–67. https://doi.org/10.1039/9781837675838-00001
14. Y. Zhang, X. Xu, Modeling of lattice parameters of cubic perovskite oxides and halides. Heliyon **7**, e07601 (2021). https://doi.org/10.1016/j.heliyon.2021.e07601
15. Y. Zhang, X. Xu, Predicting lattice parameters for orthorhombic distorted-perovskite oxides via machine learning. Solid State Sci. **113**, 106541 (2021). https://doi.org/10.1016/j.solidstatesciences.2021.106541
16. H. Liu, H. Zhu, H. Yang, A low temperature synthesis of nanocrystalline spinel $NiFe_2O_4$ and its electrochemical performance as anode of lithium-ion batteries. Mater. Res. Bull. **48**, 1587–1592 (2013). https://doi.org/10.1016/j.materresbull.2012.12.072
17. P.R. Kumar, S. Mitra, Nickel ferrite as a stable, high capacity and high rate anode for Li-ion battery applications. RSC Adv. **3**, 25058–25064 (2013). https://doi.org/10.1039/c3ra44001j
18. W. Deng, S. Ci, H. Li, Z. Wen, One-step ultrasonic spray route for rapid preparation of hollow Fe_3O_4/C microspheres anode for lithium-ion batteries. Chem. Eng. J. **330**, 995–1001 (2017). https://doi.org/10.1016/j.cej.2017.08.039
19. M. Choi, S.H. Lee, J.Y. Il, J.Y. Jung, J.S. Park, W.K. Choi, S.Y. Park, H.J. Won, J.K. Moon, J. Choi, S.B. Kim, The high capacity and cycle stability of $NiFe_2O_4$ thin film

prepared by E-beam evaporation method for lithium ion batteries. J. Alloys Compd. **729**, 802–808 (2017). https://doi.org/10.1016/j.jallcom.2017.06.334

20. D. Feng, H. Yang, X. Guo, 3-Dimensional hierarchically porous $ZnFe_2O_4$/C composites with stable performance as anode materials for Li-ion batteries. Chem. Eng. J. **355**, 687–696 (2019). https://doi.org/10.1016/j.cej.2018.08.202
21. Y. Zhang, X. Xu, Machine learning lattice constants for spinel compounds. Chem. Phys. Lett. **760**, 137993 (2020). https://doi.org/10.1016/j.cplett.2020.137993
22. B.P. Hahn, J.W. Long, A.N. Mansour, K.A. Pettigrew, M.S. Osofsky, D.R. Rolison, Electrochemical Li-ion storage in defect spinel iron oxides: the critical role of cation vacancies. Energy Environ. Sci. **4**, 1495–1502 (2011). https://doi.org/10.1039/c0ee00819b
23. I.O. Alade, Y. Zhang, X. Xu, Modeling and prediction of lattice parameters of binary spinel compounds (AM2X4) using support vector regression with Bayesian optimization. New J. Chem. **45**, 15255–15266 (2021). https://doi.org/10.1039/D1NJ01523K
24. Z. Li, N. Qiao, J. Nie, J. Zhao, J. Wang, X. Feng, S. Yao, NiO/$NiFe_2O_4$ nanocubes derived from Prussian blue as anode materials for Li-ion batteries. Mater. Lett. (2020). https://doi.org/10.1016/j.matlet.2020.128077
25. R. Alcántara, M. Jaraba, P. Lavela, J.L. Tirado, J.C. Jumas, J. Olivier-Fourcade, Changes in oxidation state and magnetic order of iron atoms during the electrochemical reaction of lithium with $NiFe_2O_4$. Electrochem. Commun. **5**, 16–21 (2003). https://doi.org/10.1016/S1388-2481(02)00520-9
26. X.D. Li, W.S. Yang, F. Li, D.G. Evans, X. Duan, Stoichiometric synthesis of pure $NiFe_2O_4$ spinel from layered double hydroxide precursors for use as the anode material in lithium-ion batteries. J. Phys. Chem. Solids **67**, 1286–1290 (2006). https://doi.org/10.1016/j.jpcs.2006.01.096
27. D. Zhang, Z. Tong, G. Xu, S. Li, J. Ma, Templated fabrication of $NiFe_2O_4$ nanorods: characterization, magnetic and electrochemical properties. Solid State Sci. **11**, 113–117 (2009). https://doi.org/10.1016/j.solidstatesciences.2008.05.001
28. D. Zhou, S. Permien, J. Rana, M. Krengel, F. Sun, G. Schumacher, W. Bensch, J. Banhart, Investigation of electronic and local structural changes during lithium uptake and release of nano-crystalline $NiFe_2O_4$ by X-ray absorption spectroscopy. J. Power. Sources **342**, 56–63 (2017). https://doi.org/10.1016/j.jpowsour.2016.12.038
29. Z. Wang, X. Zhang, X. Liu, W. Zhang, Y. Zhang, Y. Li, C. Qin, W. Zhao, Z. Bakenov, Dual-network nanoporous $NiFe_2O_4$/NiO composites for high performance Li-ion battery anodes. Chem. Eng. J. (2020). https://doi.org/10.1016/j.cej.2020.124207
30. M.A.N. Zen, F.I. Haq, R. Gabriella, S.R. Putri, A.B.D. Nandiyanto, T. Kurniawan, Techno-economic analysis of the $NiFe_2O_4$ nanoparticles for vehicle battery application using the hydrothermal synthesis method. Int. J. Sustain. Trans. Technol. **4**, 29–34 (2021). https://doi.org/10.31427/IJSTT.2021.4.1.4
31. T. Zhang, H. Cao, J. Peng, Q. Xiao, Z. Li, G. Lei, Excellent cycling performance of three-dimensional-ordered macroporous nife 2O4 as anode material for lithium ion batteries. Funct. Mater. Lett. **4**, 327–331 (2011). https://doi.org/10.1142/S1793604711002196
32. N. Karthigayan, P. Manimuthu, M. Priya, S. Sagadevan, Synthesis and characterization of $NiFe_2O_4$, $CoFe_2O_4$ and $CuFe_2O_4$ thin films for anode material in Li-ion batteries. Nanomater. Nanotechnol. (2017). https://doi.org/10.1177/1847980417711084
33. Y. Ding, Y. Yang, H. Shao, One-pot synthesis of $NiFe_2O_4$/C composite as an anode material for lithium-ion batteries. J. Power. Sources **244**, 610–613 (2013). https://doi.org/10.1016/j.jpowsour.2013.01.043
34. E.K. Heidari, B. Zhang, M.H. Sohi, A. Ataie, J.K. Kim, Sandwich-structured graphene-$NiFe_2O_4$-carbon nanocomposite anodes with exceptional electrochemical performance for Li ion batteries. J. Mater. Chem. A **2**, 8314–8322 (2014). https://doi.org/10.1039/c4ta00507d
35. Y. Zhang, J. Liu, G. Guo, Z. Lin, Review and prospect of $NiFe_2O_4$-based materials for Li-ion battery. IOP Conf. Ser. Earth Environ. Sci. **555**, 012040 (2020). https://doi.org/10.1088/1755-1315/555/1/012040
36. K.M. Naik, A. Kumar Chourasia, C.S. Sharma, Nano-interface engineering of $NiFe_2O_4$/MoS_2/MWCNTs heterostructure catalyst as cathodes in the long-Life reversible Li-CO_2 mars batteries. Chem. Eng. J. (2024). https://doi.org/10.1016/j.cej.2024.151729
37. R. Jin, H. Jiang, Y. Sun, Y. Ma, H. Li, G. Chen, Fabrication of $NiFe_2O_4$/C hollow spheres constructed by mesoporous nanospheres for high-performance lithium-ion batteries. Chem. Eng. J. **303**, 501–510 (2016). https://doi.org/10.1016/j.cej.2016.06.032
38. Z. Deng, Q. Wei, G. Wan, G. Zhao, S. Shi, P. Mou, S. Teng, C. Du, G. Wang, Synergistic effect of nanosheet structure and carbon coating engineering to enhance lithium storage performance of molybdenum niobium oxides. Mater. Today Sustain. **19**, 100176 (2022). https://doi.org/10.1016/j.mtsust.2022.100176
39. S. Shi, G. Wang, G. Wan, Y. Tang, G. Zhao, Z. Deng, J. Chai, C. Wei, G. Wang, Titanium niobate ($Ti_2Nb_{10}O_{29}$) anchored on nitrogen-doped carbon foams as flexible and

self-supported anode for high-performance lithium ion batteries. J. Colloid Interface Sci. **587**, 622–632 (2021). https://doi.org/10.1016/j.jcis.2020.11.019

40. S. Shi, Y. Tang, G. Wang, W. Yu, G. Wan, L. Wu, Z. Deng, G. Wang, Multiple reinforcement effect induced by gradient carbon coating to comprehensively promote lithium storage performance of $Ti_2Nb_{10}O_{29}$. Nano Energy **96**, 107132 (2022). https://doi.org/10.1016/j.nanoen.2022.107132
41. P. Pazhamalai, V. Krishnan, M.S. Mohamed Saleem, S.-J. Kim, H.-W. Seo, Investigating composite electrode materials of metal oxides for advanced energy storage applications. Nano Converg. **11**, 30 (2024). https://doi.org/10.1186/s40580-024-00437-2
42. S.M. Abbas, R.U.A. Zia-ur-Rehman, S.U.-D. Khan, Z. Iqbal, N. Ahmad, MoN-decorated nitrogen doped carbon nanotubes anode with high lithium storage performance. Electrochim. Acta **190**, 988–996 (2016). https://doi.org/10.1016/j.electacta.2015.12.147
43. L. Zhan, X. Ning, X. Zhou, J. Luo, X. Fan, Flower-like Bi_2S_3/rGO modified separator for lithium-sulfur batteries. Adv. Powder Technol. **33**, 103521 (2022). https://doi.org/10.1016/J.APT.2022.103521
44. X. Fan, R. Zhong, Y. Huang, X. Zhou, X. Zhu, L. Zhan, X. Zhou, Y.H. Wang, X. Wang, Oxygen defect-rich MnOOH nanorod as an effective modulator to boost polysulfide reaction kinetic for high-performance lithium sulfur battery. Appl. Surf. Sci. **614**, 155869 (2023). https://doi.org/10.1016/J.APSUSC.2022.155869
45. J. Tang, X. Zhou, B. Jin, J. Luo, X. Ning, L. Zhan, Z. Wu, X. Fan, G. Wang, X. Zhou, Microwave-assisted synthesis of a ternary MoS_2/carbon-FeOx composites with 3D hierarchical nanostructure for lithium-ion battery application. J. Mater. Sci. **34**, 121 (2023). https://doi.org/10.1007/s10854-022-09553-3
46. L. Zhan, X. Zhou, J. Luo, X. Ning, Ion assisted anchoring Sn nanoparticles on nitrogen-doped graphene as an anode for lithium ion batteries. Int. J. Hydrogen Energy **44**, 24913–24921 (2019). https://doi.org/10.1016/J.IJHYDENE.2019.07.153
47. L. Zhan, X. Zhou, J. Luo, X. Ning, Binder-free multilayered SnO_2/graphene on Ni foam as a high-performance lithium ion batteries anode. Ceram. Int. **45**, 6931–6936 (2019). https://doi.org/10.1016/J.CERAMINT.2018.12.190
48. P.R. Anusuyadevi, Z.S. Campbell, A. Erriguible, S. Marre, C. Aymonier, Supercritical millifluidic reactor for the synthesis of efficient GaN nanophotocatalysts. Chem. Eng. J. Adv. **14**, 100483 (2023). https://doi.org/10.1016/j.ceja.2023.100483
49. S. Pan, X. Zhao, Nitrogen-doped graphene supported $NiFe_2O_4$ nanoparticles as high-performance anode material for lithium-ion batteries. J. Mater. Sci. **32**, 26917–26928 (2021). https://doi.org/10.1007/s10854-021-07066-z
50. ICDD 98-011-6755
51. H. Zhao, Z. Zheng, K.W. Wong, S. Wang, B. Huang, D. Li, Fabrication and electrochemical performance of nickel ferrite nanoparticles as anode material in lithium ion batteries. Electrochem. Commun. **9**, 2606–2610 (2007). https://doi.org/10.1016/j.elecom.2007.08.007
52. F. Lai, X. Zhang, Q. Wu, J. Zhang, Q. Li, Y. Huang, Z. Liao, H. Wang, Effect of surface modification with spinel $NiFe_2O_4$ on enhanced cyclic stability of $LiMn_2O_4$ cathode material in lithium ion batteries. ACS Sustain. Chem. Eng. **6**, 570–578 (2018). https://doi.org/10.1021/acssuschemeng.7b02876
53. R. Sivakami, S. Dhanuskodi, R. Karvembu, Estimation of lattice strain in nanocrystalline RuO_2 by Williamson-Hall and size–strain plot methods. Spectrochim. Acta A **152**, 43–50 (2016). https://doi.org/10.1016/j.saa.2015.07.008
54. A.A. Al-Tabbakh, N. Karatepe, A.B. Al-Zubaidi, A. Benchaabane, N.B. Mahmood, Crystallite size and lattice strain of lithiated spinel material for rechargeable battery by X-ray diffraction peak-broadening analysis. Int. J. Energy Res. **43**, 1903–1911 (2019). https://doi.org/10.1002/er.4390
55. R. Singh Yadav, J. Havlica, J. Masilko, L. Kalina, J. Wasserbauer, M. Hajdúchová, V. Enev, I. Kuřitka, Z. Kožáková, Effects of annealing temperature variation on the evolution of structural and magnetic properties of $NiFe_2O_4$ nanoparticles synthesized by starch-assisted sol-gel auto-combustion method. J. Magn. Magn. Mater. **394**, 439–447 (2015). https://doi.org/10.1016/j.jmmm.2015.07.012
56. R.S. Yadav, I. Kuřitka, J. Vilcakova, J. Havlica, J. Masilko, L. Kalina, J. Tkacz, V. Enev, M. Hajdúchová, Structural, magnetic, dielectric, and electrical properties of $NiFe_2O_4$ spinel ferrite nanoparticles prepared by honey-mediated sol-gel combustion. J. Phys. Chem. Solids **107**, 150–161 (2017). https://doi.org/10.1016/j.jpcs.2017.04.004
57. M. Parishani, M. Nadafan, Z. Dehghani, R. Malekfar, G.H.H. Khorrami, Optical and dielectric properties of $NiFe_2O_4$ nanoparticles under different synthesized temperature. Results Phys. **7**, 3619–3623 (2017). https://doi.org/10.1016/J.RINP.2017.09.049
58. M. Ebrahimi, M. Ghasemi, V. Soleimanian, M. Nekoeinia, A. Mokhtari, Effects of annealing temperature on microstructural, optical and FTIR properties of $NiFe_2O_4$ spinel nanoparticles. Chem. Phys. Lett. **833**, 140911 (2023). https://doi.org/10.1016/J.CPLETT.2023.140911
59. J. Jacob, M.A. Khadar, Investigation of mixed spinel structure of nanostructured nickel ferrite. J. Appl. Phys. (2010). https://doi.org/10.1063/1.3429202

60. P. Chandramohan, M.P. Srinivasan, S. Velmurugan, S.V. Narasimhan, Cation distribution and particle size effect on Raman spectrum of $CoFe_2O_4$. J. Solid State Chem. **184**, 89–96 (2011). https://doi.org/10.1016/j.jssc.2010.10.019
61. X. Gao, W. Wang, J. Bi, Y. Chen, X. Hao, X. Sun, J. Zhang, Morphology-controllable preparation of $NiFe_2O_4$ as high performance electrode material for supercapacitor. Electrochim. Acta **296**, 181–189 (2019). https://doi.org/10.1016/j.electacta.2018.11.054
62. M.M. Titirici, M. Antonietti, A. Thomas, A generalized synthesis of metal oxide hollow spheres using a hydrothermal approach. Chem. Mater. **18**, 3808–3812 (2006). https://doi.org/10.1021/cm052768u
63. C. Pan, D. Zhang, L. Shi, CTAB assisted hydrothermal synthesis, controlled conversion and CO oxidation properties of CeO_2 nanoplates, nanotubes, and nanorods. J. Solid State Chem. **181**, 1298–1306 (2008). https://doi.org/10.1016/j.jssc.2008.02.011
64. A.J. Cornet, A.M. Homborg, P.R. Anusuyadevi, L. Hoen-Velterop, J.M.C. Mol, Unravelling corrosion degradation of aged aircraft components protected by chromate-based coatings. Eng. Fail. Anal. (2024). https://doi.org/10.1016/j.engfailanal.2024.108070
65. Thermo Fisher Scientific (2024) Adventitious carbon contamination. In: Thermo Fisher Scientific Inc. https://www.thermofisher.com/nl/en/home/materials-science/learning-center/periodic-table/non-metal/carbon.html. Accessed 12 May 2024
66. Z. Wu, Z. Zou, J. Huang, F. Gao, $NiFe_2O_4$ nanoparticles/NiFe layered double-hydroxide nanosheet heterostructure array for efficient overall water splitting at large current densities. ACS Appl. Mater. Interfaces **10**, 26283–26292 (2018). https://doi.org/10.1021/acsami.8b07835
67. Y. He, L. Zhang, H.W. Xiong, X. Kang, Evolution of lattice defects in nickel ferrite spinel: oxygen vacancy and cation substitution. J. Alloys Compd. (2022). https://doi.org/10.1016/j.jallcom.2022.165494
68. K. Jouini, A. Raouafi, W. Dridi, M. Daoudi, B. Mustapha, R. Chtourou, F. Hosni, Investigation of gamma-ray irradiation induced phase change from NiO to Ni_2O_3 for enhancing photocatalytic performance. Optik (Stuttg) (2019). https://doi.org/10.1016/j.ijleo.2019.163109
69. G. Xie, Y. Sakamura, K. Ema, Y. Ito, Characterization of nickel oxide in molten carbonate I. Electrochemical behaviour of higher nickel oxide in molten carbonate. J. Power. Sources **32**, 125–133 (1990). https://doi.org/10.1016/S0378-7753(12)80002-4
70. ALOthman Z, A review: fundamental aspects of silicate mesoporous materials. Materials **5**, 2874–2902 (2012). https://doi.org/10.3390/ma5122874
71. J. Wang, G. Yang, W. Lyu, W. Yan, Thorny TiO_2 nanofibers: synthesis, enhanced photocatalytic activity and supercapacitance. J. Alloys Compd. **659**, 138–145 (2016). https://doi.org/10.1016/j.jallcom.2015.10.233
72. K.S.W. Sing, Reporting physisorption data for gas/solid systems with special reference to the determination of surface area and porosity (Recommendations 1984). Pure Appl. Chem. **57**, 603–619 (1985). https://doi.org/10.1351/pac198557040603
73. Y. Yamaguchi, R. Aono, E. Hayashi, K. Kamata, M. Hara, Template-free synthesis of mesoporous β-MnO_2 nanoparticles: structure, formation mechanism, and catalytic properties. ACS Appl. Mater. Interfaces **12**, 36004–36013 (2020). https://doi.org/10.1021/acsami.0c08043
74. M. Islam, G. Ali, M.G. Jeong, W. Choi, K.Y. Chung, H.G. Jung, Study on the electrochemical reaction mechanism of $NiFe_2O_4$ as a high-performance anode for Li-ion batteries. ACS Appl. Mater. Interfaces **9**, 14833–14843 (2017). https://doi.org/10.1021/acsami.7b01892
75. U. Kasavajjula, C. Wang, A.J. Appleby, Nano- and bulk-silicon-based insertion anodes for lithium-ion secondary cells. J. Power. Sources **163**, 1003–1039 (2007). https://doi.org/10.1016/j.jpowsour.2006.09.084
76. A.S. Aricò, P. Bruce, B. Scrosati, J.-M. Tarascon, W. van Schalkwijk, Nanostructured materials for advanced energy conversion and storage devices. Nat. Mater. **4**, 366–377 (2005). https://doi.org/10.1038/nmat1368
77. H. Bashirpour-bonab, Investigation and electrochemical analysis of SEI layer formation in natural graphite anode formation process in lithium-ion battery. E-Prime **5**, 100261 (2023). https://doi.org/10.1016/j.prime.2023.100261
78. S.J. An, J. Li, C. Daniel, D. Mohanty, S. Nagpure, D.L. Wood, The state of understanding of the lithium-ion-battery graphite solid electrolyte interphase (SEI) and its relationship to formation cycling. Carbon NY **105**, 52–76 (2016). https://doi.org/10.1016/j.carbon.2016.04.008
79. A. Wang, S. Kadam, H. Li, S. Shi, Y. Qi, Review on modeling of the anode solid electrolyte interphase (SEI) for lithium-ion batteries. NPJ Comput. Mater. **4**, 15 (2018). https://doi.org/10.1038/s41524-018-0064-0
80. E. Riyanto, T. Kristiantoro, E. Martides, P.B. Dedi, D. Mulyadi, Suprapto, Lithium-ion battery performance improvement using two-dimensional materials. Mater. Today Proc. **87**, 164–171 (2023). https://doi.org/10.1016/j.matpr.2023.02.392
81. A.R.C. Bredar, A.L. Chown, A.R. Burton, B.H. Farnum, Electrochemical impedance spectroscopy of metal oxide electrodes for energy applications. ACS Appl. Energy

Mater. **3**, 66–98 (2020). https://doi.org/10.1021/acsaem.9b01965

82. J.Y. Xiang, J.P. Tu, Y.Q. Qiao, X.L. Wang, J. Zhong, D. Zhang, C.D. Gu, Electrochemical impedance analysis of a hierarchical cuo electrode composed of self-assembled nanoplates. J. Phys. Chem. C **115**, 2505–2513 (2011). https://doi.org/10.1021/jp108261t
83. C. Wang, Q. Li, F. Wang, G. Xia, R. Liu, D. Li, N. Li, J.S. Spendelow, G. Wu, Morphology-dependent performance of CuO anodes via facile and controllable synthesis for lithium-ion batteries. ACS Appl. Mater. Interfaces **6**, 1243–1250 (2014). https://doi.org/10.1021/am405061c
84. P.C. Rath, J. Patra, D. Saikia, M. Mishra, C.M. Tseng, J.K. Chang, H.M. Kao, Comparative study on the morphology-dependent performance of various CuO nanostructures as anode materials for sodium-ion batteries. ACS Sustain. Chem. Eng. **6**, 10876–10885 (2018). https://doi.org/10.1021/acssuschemeng.8b02159
85. M.D. Levi, D. Aurbach, Simultaneous measurements and modeling of the electrochemical impedance and the cyclic voltammetric characteristics of graphite electrodes doped with lithium. J. Phys. Chem. B **101**, 4630–4640 (1997). https://doi.org/10.1021/jp9701909

Publisher's Note Springer Nature remains neutral with regard to jurisdictional claims in published maps and institutional affiliations.